

Programmable artificial intelligence machine for wave sensing and communications

Tie Jun Cui (✉ tjcui@seu.edu.cn)

Southeast University <https://orcid.org/0000-0002-5862-1497>

Che Liu

Southeast University <https://orcid.org/0000-0002-9917-8487>

qian ma

Southeast University

Zhangjie Luo

Institute of Electromagnetic Space; State Key Laboratory of Millimeter Wave

Qiaoru Hong

Institute of Electromagnetic Space; State Key Laboratory of Millimeter Wave

Qiang Xiao

Southeast University

Hao Chi Zhang

Southeast University <https://orcid.org/0000-0002-9856-5848>

Long Miao

Jiangsu Cyber-Space Science & Technology Co., Ltd.

Wenming Yu

Institute of Electromagnetic Space; State Key Laboratory of Millimeter Wave

Qiang Cheng

Southeast University

Lianlin Li

peking university <https://orcid.org/0000-0001-9394-3638>

Physical Sciences - Article

Keywords: Artificial intelligence, AI, human life, convenient

Posted Date: October 19th, 2020

DOI: <https://doi.org/10.21203/rs.3.rs-90701/v1>

License: © ⓘ This work is licensed under a Creative Commons Attribution 4.0 International License.

[Read Full License](#)

Version of Record: A version of this preprint was published at Nature Electronics on February 21st, 2022.
See the published version at <https://doi.org/10.1038/s41928-022-00719-9>.

Programmable artificial intelligence machine for wave sensing and communications

Che Liu^{1,2,†}, Qian Ma^{1,2,†}, Zhang Jie Luo^{1,2}, Qiao Ru Hong^{1,2}, Qiang Xiao^{1,2}, Hao Chi Zhang^{1,2}, Long Miao³, Wen Ming Yu^{1,2,3}, Qiang Cheng^{1,2}, Lianlin Li⁴, and Tie Jun Cui^{1,2,*}

¹ Institute of Electromagnetic Space, Southeast University, Nanjing 210096, China.

² State Key Laboratory of Millimeter Wave, Southeast University, Nanjing 210096, China.

³ Jiangsu Cyber-Space Science & Technology Co., Ltd., 12 Mozhou East Road, Nanjing 211111, China.

⁴ School of Electronic Engineering and Computer Sciences, Peking University, Beijing 100871, China.

*Correspondence to: tjcui@seu.edu.cn.

† Che Liu and Qian Ma: These authors contributed equally to this work.

Abstract: Artificial intelligence is facilitating human life in many aspects. Previous artificial intelligence has been mainly focused on computer algorithms (e.g. deep-learning and extreme-learning) and integrated circuits. Recently, all-optical diffractive deep neural networks (D²NN) were realized by using passive structures, which can perform complicated functions designed by computer-based neural networks at the light speed. However, once a passive D²NN architecture is fabricated, its function will be fixed. Here, we propose a programmable artificial intelligence machine (PAIM) that can execute various intellectual tasks by realizing hierarchical connections of brain neurons via a multi-layer digital-coding metasurface array. Integrated with two amplifier chips in each meta-atom, its transmission coefficient covers a dynamic range of 35 dB (from -40 dB to -5 dB), which is the basis to construct the reprogrammable physical layers of D²NN, in which the digital meta-atoms make the artificial neurons *alive*. We experimentally show that PAIM can handle various deep-learning tasks for wave sensing, including image classifications, mobile communication coder-decoder, and real-time multi-beam focusing. In particular, we propose a reinforcement learning algorithm for on-site learning and discrete optimization algorithm for digital coding, making PAIM have autonomous intelligence ability and perform self-learning tasks without the support of extra computer.

One Sentence Summary: A programmable artificial intelligence machine composed of multiple digital coding metasurfaces driven by wave-based calculations at the light speed can execute various deep-learning and on-site reinforcement learning tasks for wave sensing and communications.

Main Text:

Artificial intelligence (AI) has been making human life more convenient through various applications. Currently, there are two main technical streams in AI science, one of which is the computer-based machine learning methods such as deep learning¹, extreme learning², and reinforcement learning³; while the other is based on the integrated circuits and optical chips⁴⁻⁷. AI is generally realized by using hierarchical artificial neural networks (ANNs) to imitate the structure of neurons in human brain¹ and simulate the intelligent actions in human decision-making process, and hence has found wide applications in face recognition^{8,9} automatic driving^{10,11}, language processing^{12,13}, and medical diagnostics^{14,15}. Besides the computer-based and circuit-based AI technologies, all wave-based ANNs have recently been presented using three-dimensional (3D) printed optical lens arrays¹⁶. Rather than using the traditional computer platforms to implement ANNs, the optical platform (also called as diffractive deep neural networks, D²NN) could take advantage of the wave property of photons to realize parallel calculations and simulate different interconnection structures at the speed of light¹⁶⁻¹⁸. However, the wave-based D²NN is still a passive device, which has fixed network architecture once fabricated. Hence it cannot be re-trained for other targets, limiting its functionalities and applications. In addition, this wave-based D²NN platform still relies on computer to optimize the parameters and requires prior information of environment.

To establish a re-trainable wave-based D²NN, a weight-reprogrammable node is necessary to make the neurons *alive*. This is possible to achieve using programmable metasurface¹⁹ and information metasurface²⁰. In the past decade, metamaterials and metasurfaces have been well developed for manipulating lights and electromagnetic (EM) waves²¹⁻²⁴. The digital-coding representation of meta-atoms makes the information metasurface be reprogrammable and sets up a direct connection between the physical world and digital world^{19,20,25,26}. With controllable active components, the programmable metasurface can manipulate the reflected or transmitted EM waves in real time under the digital instruction from field-programmable gate array (FPGA). Various functions and applications have been achieved using the information metasurfaces, including new-architecture wireless communications²⁷⁻²⁹, imaging³⁰, space-time modulation³¹, and smart devices³².

Here, we propose a programmable and on-site trainable artificial intelligence machine (PAIM) using an array of information metasurfaces for wave sensing and communications, in which the multi-layer metasurfaces act as the programmable physical layers of D²NN. We design our PAIM to be a real-time re-trainable system, whose parameters could be set in digital to realize *alive* artificial neurons. In the physical layer, PAIM could hierarchically manipulate the energy distribution of transmitted EM waves by a five-layer information metasurface array^{33,34}, from which the amplitude of transmitted wave through each meta-atom could be enhanced or attenuated by controlling the value of digital parameters (Fig. 1a). The phase change of the transmitted wave is determined by the phase part of complex-valued gain factor of the programmable meta-atom, which is also modulated by the customized FPGA circuit (Fig. 3b, Supplementary Fig. S1, Supplementary Materials Note 1 'FPGA Modulation and Feedback Channels of Receivers'). When the incident beam goes through a programmable meta-atom in the first-layer metasurface, the amplitude and phase of transmitted wave are determined by the product of incident electric field and complex-valued transmission coefficient of the meta-atom, and the transmitted wave will act as a secondary source and illuminate on all programmable meta-atoms in the second-layer metasurface (Fig. 1b, c), based on the Huygens-Fresnel principle¹⁶. Then the transmitted waves from all directions illuminate on a meta-atom in the

second layer are added up and the whole will act as the incident wave to the meta-atom in the second-layer metasurface (Fig. 1b). This process is continued until to the final layer. Here, the reprogrammable interconnection architectures in PAIM is the fundamental and essential factor to simulate the *alive* artificial neurons.

According to the radiation pattern of meta-atom (Fig. 1d), the power transmitted by the meta-atom has a certain weight distribution on the next-layer metasurface (Fig. 1c). Therefore, the forward propagation model (see Supplementary Materials Note 3 ‘Forward Propagation Model’) of PAIM can be regarded as a fully-connected network (Supplementary Fig. S2). However, compared with the traditional fully-connected network constructed by real numbers¹, the PAIM parameters have complex values and the trainable parts are complex-valued transmission coefficients of the meta-atoms. Hence, we have fewer trainable parameters (Supplementary Fig. S2). The traditional error back-propagation method could be used to train the PAIM parameters. Meanwhile, owing to the fast parameter-switching ability and direct feedback from receivers (Supplementary Fig. S1), our PAIM enables self-learning capability by using the data gained from the direct interaction with environment, and does not need any prior knowledge. Thus, PAIM possesses the reinforcement learning capacity³⁵.

When processing given data, we make the first-layer programmable metasurface as a digital-analog converter to modulate the given data into the amplitude distribution of EM wave when illuminated by plane waves (Fig. 1a, b). Then, the transmitted EM waves carry the information of given data and will be processed by remaining metasurface layers. Therefore, without using independent and complicated input modules, PAIM is more flexible and compact than the optical D²NN platforms^{16,36,37}. In fact, PAIM can directly receive and process the EM waves radiated by radars, communication base stations, and wireless routers, making it more environment compatible.

To verify the powerful capabilities of PAIM, we firstly use it to deal with two image classification tasks: oil painting style (Fig. 1e, g, Supplementary Fig. S4) and handwritten digit (Supplementary Fig. S3) classifications. In the first classification task with two kinds of oil paintings (portraiture and landscape painting), we simulate a PAIM with 6-layer metasurfaces, each of which consists of 25×25 programmable meta-atoms. The input image (Fig. 1e) is grayed and reshaped to 25×25 pixels (corresponding to the size of metasurface) (Fig. 1f), and then inputted to PAIM by configuring the first-layer metasurface, in which the transmission coefficient of each meta-atom is set as the corresponding pixel value of the image. Thus, the EM wave would carry the information of the input image when going through the first layer. The remaining five layers constitute the recognition network. At the end of PAIM, we assign 2 receivers to get the 2 kinds of oil paintings. The receiving energy at each receiver represents the level of possibility that the input image is classified. The receiver with the maximum receiving energy corresponds to the kind of classification result (Fig. 1g). After training with 500 handwritten digit images and testing with 100 images, the mean accurate rate to recognize the two oil painting styles is 97%. We remark that the number of trainable parameters is only 5×25×25, which is much fewer than that in the traditional fully-connected ANN networks. The similar architecture is used in handwritten digit classification with the layer size of 40×40, in which the handwritten digits are classified into ten different kinds, reaching a 90.76% classification accuracy after training (Supplementary Fig. S3). More details on the network design and recognition results are provided in Supplementary Materials.

For demonstrating the versatility of our PAIM in real world, we design and fabricate a PAIM sample with five-layer programmable metasurfaces controlled by five FPGA modules, and each layer consists of 8×8 meta-atoms (Figs. 1a, 3b). Each meta-atom integrated with two amplifiers (Supplementary Fig. S5) can modulate more than 500 different grades of transmitted gain of the EM wave (Supplementary Fig. S6) individually under the control of bias voltage by FPGA, imitating as an alive neuron in the fully connected network. The support structure of the PAIM sample is presented in Supplementary Fig. S7, in which the first layer (i.e., the input layer) is illuminated by microwaves at 5.4 GHz radiated by a horn antenna. The measurement is performed in a standard microwave chamber (Supplementary Fig. S8c, d).

To test the real experimental performance of PAIM in image classification, we design two imaginative cases. One case is to classify simple patterns, and the other is to recognize four kinds of game props in a popular sandbox game ‘**Minecraft**’. As mentioned above, the first-layer metasurface of PAIM acts as a digital-to-analog converter to convert the input image into the corresponding spatial distribution of EM waves. More specifically, different pixel values in the input image correspond to different transmission coefficients of the meta-atoms in the first layer, radiating EM waves with different spatial distributions onto the second layer. The remaining four layers act as a recognizer, and several receiving antennas are put at the end of PAIM. The training process is run in a computer to obtain appropriate transmission coefficients of the meta-atoms in the recognizer. A gradient back propagation algorithm could be used to train PAIM. However, considering the fact that the adjustable parameters of digital coding metasurfaces are discrete, we specially design a discrete optimization algorithm to make the training results more practical. Meanwhile, we calibrate the wave propagation coefficients between two adjacent metasurface layers using a gradient decent method to make our training results more precise. More details on the discrete optimization algorithm and calibration approach are provided in the Supplementary Materials.

In our first experimental image classification, we design two simple patterns, letter ‘I’ and bracket ‘[]’. The positions of such patterns could be different to make the input images more variegated. The pixels belonging to pattern parts and background are allocated with different bias voltages of meta-atoms in the first PAIM layer. Experimental results show that our PAIM could classify the two patterns with an accuracy of 100% (Fig. 2a-d, Supplementary Fig. S9). In the second case of game prop recognition, we choose four kinds of classical props: pickaxe, handgun, sword, and axe. We down-sample the original prop image into an 8×8 pixel matrix and use different bias voltages of meta-atoms in the first PAIM layer to represent different pixel values. The bias-voltage configurations of layers 2-5 (corresponding to the recognition part of PAIM) for this case are shown in Fig. 2I. 100% recognition accuracy is also achieved in the experimental tests (Fig. 2e-h, Supplementary Fig. S10).

Besides the image classification, we further use PAIM for mobile communication codec, which can perform coding and decoding tasks in Code Division Multiple Access (CDMA) scheme, and transmit four kinds of orthogonal user codes simultaneously or separately in one channel. Here, each user code is a string of binary numbers with length of 64. As shown in Fig. 3a, the first-layer PAIM metasurface is set as an encoder, on which each meta-atom sequentially corresponds to one bit in the binary number string. When high or low bias voltage is set to the meta-atom, it will correspond to ‘1’ or ‘0’ bit, respectively. We put four receiving antennas at the end of PAIM, and each antenna

represents a user code. When one of the antennas receives high energy of EM waves, it means that the corresponding user code related to this antenna is transmitted (Fig. 3a).

We use $\{C_1, C_2, C_3, C_4\}$ to represent the four user codes, and $\{E_1, E_2, E_3, E_4\}$ to represent the receiving energies of the corresponding antennas. The remaining four-layer PAIM metasurfaces are trained as a decoder. When C_1 is transmitted by the first layer, the values of $\{E_1, E_2, E_3, E_4\}$ would be $f(C_1) = \{high, low, low, low\}$, in which the function f represents the linear forward propagation function of PAIM, and the term *low* indicates that the receiving energy is much less than that of *high*. Similarly, when C_3 is transmitted, the receiving energy values would be

$f(C_3) = \{low, low, high, low\}$. For a more complicated situation, when C_1 and C_3 are transmitted simultaneously, the receiving energy values would be:

$f(C_1 + C_3) = f(C_1) + f(C_3) = \{high, low, high, low\}$. The same is true when three or four user codes are transmitted simultaneously. Owing to the independence of wave propagation, the transmission of one user code has little influence on the transmission of others, and hence each user code could be transmitted nearly independently in one channel.

This property allows simplification of the training process: we do not need to train all combinations of the four user codes. Instead, when the output EM wave distribution of each user code conforms to the designed distribution, the combinations would satisfy the expectation automatically. The total loss function for training is the sum of mean square errors (MSEs) between the designed output energy distribution and the generated one by inputting each of the four user codes. Random Gaussian noise is added to the training input to make our system more robust. The experimental results verify the feasibility of PAIM in wireless communications (Fig. 3c-f, Supplementary Fig. S11). Compared with the traditional CDMA scheme, our PAIM performs coding and decoding using space dimension instead of time dimension, and realizes the Open System Interconnection (OSI) reference model in the physical layer instead of link layer (Supplementary Fig. S12). Therefore, PAIM has the advantage to reduce the time delay in wireless communications. On the other hand, the strong capability of processing distributed space EM waves makes PAIM a good candidate to realize space division multiplexing and thus increases the channel capacity. The decoding function of PAIM is operated as a dependent system and is able to deal with signals from distributed communication base stations (Supplementary Fig. S13). In fact, with the exhaustion of spectrum resources, the space division multiplexing technique has obtained increasing attention and becomes the key technology in the fifth and sixth generations of wireless communications³⁸.

Finally, we turn our PAIM into a dynamic multi-beam focusing lens, which could focus the EM energy on multiple points with arbitrary positions. Different from the aforementioned cases, in which the training process is executed on a computer in advance, here we directly make on-site training to PAIM using reinforce-learning method in real time, which completely overcomes the limitation to require priori knowledge in the previous optical D²NN platforms. Benefit from the real-time programmable ability of PAIM, we can train the parameters by continuously interacting with

unknown and complicated EM environment. Figure 4a illustrates the schematic diagram of the reinforce-learning process, in which the bias voltages of meta-atoms are randomly changed and controlled by FPGA. The same FPGA also receives the feedback signals from receivers and calculates the trend of error function to determine whether the change of bias voltages is reserved or eliminated. In this case, MSE is used as the error function again, and an extra function is added to restrain the redundant EM waves (see Supplementary Materials Note 2 ‘Reinforce-Learning Process’). It could be regarded as a real-time optimization procedure, and the optimal objective is minimizing the distance between the desired pattern and the generated EM wave distribution by PAIM. The output EM wave distributions along with the updated times of parameters are presented in Fig. 4b, c. After the automatic training, PAIM could transform the output EM waves into the target point(s) with more than 90% concentrated energy, and the focusing point(s) could shift with a frequency of 100 Hz to realize multi-beam scanning. In this application, benefit from the real-time updates of parameters in PAIM, no extra training dataset is needed. The experimental results indicate that PAIM could apply for different kinds of EM environments.

In conclusion, the proposed PAIM is an on-site programmable D²NN platform running by real-time control of EM waves in digital way, which can perform computations based on the parallelism of EM wave propagations at the speed of light. It is a universe wave-based intelligence machine, which can not only deal with the traditional deep learning tasks such as image recognition and feature detection, but also provide on-site and user-friendly way to manipulate the spatial EM waves such as multi-channel coding and decoding in the CDMA scheme and dynamic multi-beam focusing, and hence may find new applications in the wireless communications, signal enhancement, medical imaging, remote control, internet of things (IoT), and other intelligent applications.

References

- 1 Lecun, Y., Bengio, Y. & Hinton, G. Deep learning. *Nature* **521**, 436-444 (2015).
- 2 Huang, G., Huang, G. B., Song, S. J. & You, K. Y. Trends in extreme learning machines: A review. *Neural Networks* **61**, 32-48 (2015).
- 3 Mnih, V. *et al.* Human-level control through deep reinforcement learning. *Nature* **518**, 529-533 (2015).
- 4 Ren, H. R., Li, X. P., Zhang, Q. M. & Gu, M. On-chip noninterference angular momentum multiplexing of broadband light. *Science* **352**, 805-809 (2016).
- 5 Shen, Y. *et al.* Deep learning with coherent nanophotonic circuits. *Nature Photonics* **11**, 441-446 (2017).
- 6 Hughes, T. W., Minkov, M., Shi, Y. & Fan, S. Training of photonic neural networks through in situ backpropagation and gradient measurement. *Optica* **5**, 864-871 (2018).
- 7 Feldmann, J., Youngblood, N., Wright, C. D., Bhaskaran, H. & Pernice, W. H. P. All-optical spiking neurosynaptic networks with self-learning capabilities. *Nature* **569**, 208-214 (2019).
- 8 Wright, J., Yang, A. Y., Ganesh, A., Sastry, S. S. & Ma, Y. Robust face recognition via sparse representation. *IEEE Transactions on Pattern Analysis and Machine Intelligence* **31**, 210-227 (2009).
- 9 Ding, C., Choi, J., Tao, D. & Davis, L. S. Multi-Directional multi-level dual-cross patterns for robust face recognition. *Ieee Transactions on Pattern Analysis and Machine Intelligence* **38**, 518-531 (2016).

- 10 Vazifeh, M. M., Santi, P., Resta, G., Strogatz, S. H. & Ratti, C. Addressing the minimum fleet problem in on-demand urban mobility. *Nature* **557**, 534-538 (2018).
- 11 Li, W. *et al.* AADS: Augmented autonomous driving simulation using data-driven algorithms. *Science Robotics* **4**, eaaw0863, (2019).
- 12 Palangi, H. *et al.* Deep sentence embedding using long short-term memory networks: analysis and application to information retrieval. *IEEE-Acm Transactions on Audio Speech and Language Processing* **24**, 694-707 (2016).
- 13 Young, T., Hazarika, D., Poria, S. & Cambria, E. Recent trends in deep learning based natural language processing. *IEEE Computational Intelligence Magazine* **13**, 55-75 (2018).
- 14 He, J. *et al.* The practical implementation of artificial intelligence technologies in medicine. *Nature Medicine* **25**, 30-36 (2019).
- 15 Haque, A., Milstein, A. & Fei-Fei, L. Illuminating the dark spaces of healthcare with ambient intelligence. *Nature* **585**, 193-202 (2020).
- 16 Lin, X. *et al.* All-optical machine learning using diffractive deep neural networks. *Science* **361**, 1004-1008 (2018).
- 17 Duport, F., Schneider, B., Smerieri, A., Haelterman, M. & Massar, S. All-optical reservoir computing. *Optics Express* **20**, 22783-22795 (2012).
- 18 Larger, L. *et al.* Photonic information processing beyond Turing: an optoelectronic implementation of reservoir computing. *Optics Express* **20**, 3241-3249 (2012).
- 19 Cui, T. J., Qi, M. Q., Wan, X., Zhao, J. & Cheng, Q. Coding metamaterials, digital metamaterials and programmable metamaterials. *Light-Science & Applications* **3**, e218 (2014).
- 20 Cui, T. J., Liu, S. & Zhang, L. Information metamaterials and metasurfaces. *Journal of Materials Chemistry C* **5**, 3644-3668 (2017).
- 21 Pendry, J. B., Luo, Y. & Zhao, R. K. Transforming the optical landscape. *Science* **348**, 521-524 (2015).
- 22 Qiu, C. W. & Yang, Y. J. Vortex generation reaches a new plateau. *Science* **357**, 645-645 (2017).
- 23 Hu, G. W. *et al.* Coherent steering of nonlinear chiral valley photons with a synthetic Au-WS2 metasurface. *Nature Photonics* **13**, 467-472 (2019).
- 24 Li, L. *et al.* Metalens-array-based high-dimensional and multiphoton quantum source. *Science* **368**, 1487-1490 (2020).
- 25 Cui, T. J., Li, L., Liu, S., Ma, Q. & Cheng, Q. J. i. Information metamaterial systems. *iScience* **23**, 101403 (2020).
- 26 Ma, Q. & Cui, T. J. Information Metamaterials: bridging the physical world and digital world. *Photonix* **1**, 1-32 (2020).
- 27 Zhao, J. *et al.* Programmable time-domain digital-coding metasurface for non-linear harmonic manipulation and new wireless communication systems. *National Science Review* **6**, 231-238 (2019).
- 28 Cui, T. J., Liu, S., Bai, G. D. & Ma, Q. Direct transmission of digital message via programmable coding metasurface. *Research* **2019**, 2584509 (2019).
- 29 Zhao, H. *et al.* Metasurface-assisted massive backscatter wireless communication with commodity Wi-Fi signals. *Nature communications* **11**, 3926-3926 (2020).

- 30 Li, L. L. *et al.* Electromagnetic reprogrammable coding-metasurface holograms. *Nature Communications* **8**, 197 (2017).
- 31 Zhang, L. *et al.* Space-time-coding digital metasurfaces. *Nature Communications* **9**, 4334 (2018).
- 32 Ma, Q. *et al.* Smart metasurface with self-adaptively reprogrammable functions. *Light-Science & Applications* **8**, 98 (2019).
- 33 Ma, Q. *et al.* Controllable and programmable nonreciprocity based on detachable digital coding metasurface. *Advanced Optical Materials* **7**, 1901285 (2019).
- 34 Chen, L. *et al.* Space-energy digital-coding metasurface based on an active amplifier. *Physical Review Applied* **11**, 054051(2019).
- 35 Schmidhuber, J. Deep learning in neural networks: An overview. *Neural Networks* **61**, 85-117 (2015).
- 36 Zuo, Y. *et al.* All-optical neural network with nonlinear activation functions. *Optica* **6**, 1132-1137 (2019).
- 37 Khoram, E. *et al.* Nanophotonic media for artificial neural inference. *Photonics Research* **7**, 823-827 (2019).
- 38 Zhu, J., Zhao, M., Zhang, S. & Zhou, W. Exploring the road to 6G: ABC — foundation for intelligent mobile networks. *China Communications* **17**, 51-67 (2020).

Acknowledgments: This work was supported by the National Key Research and Development Program of China (grant nos. 2017YFA0700201, 2017YFA0700202, and 2017YFA0700203).

Author contributions: T. J. C., C. L., Q. M., and L. L. conceived of the research; C. L., and Q. M. designed the PAIM devices and relevant algorithms. C. L., Q. M. and Z. J. L. contributed to the experiments; T. J. C, C. L., and Q. M. prepared the manuscript; and T. J. C. initiated and supervised the research. All authors contributed to the data analysis and writing of the manuscript, which was reviewed by all authors.

Competing interests: T. J. C, C. L., and Q. M. are inventors of a patent application on PAIM.

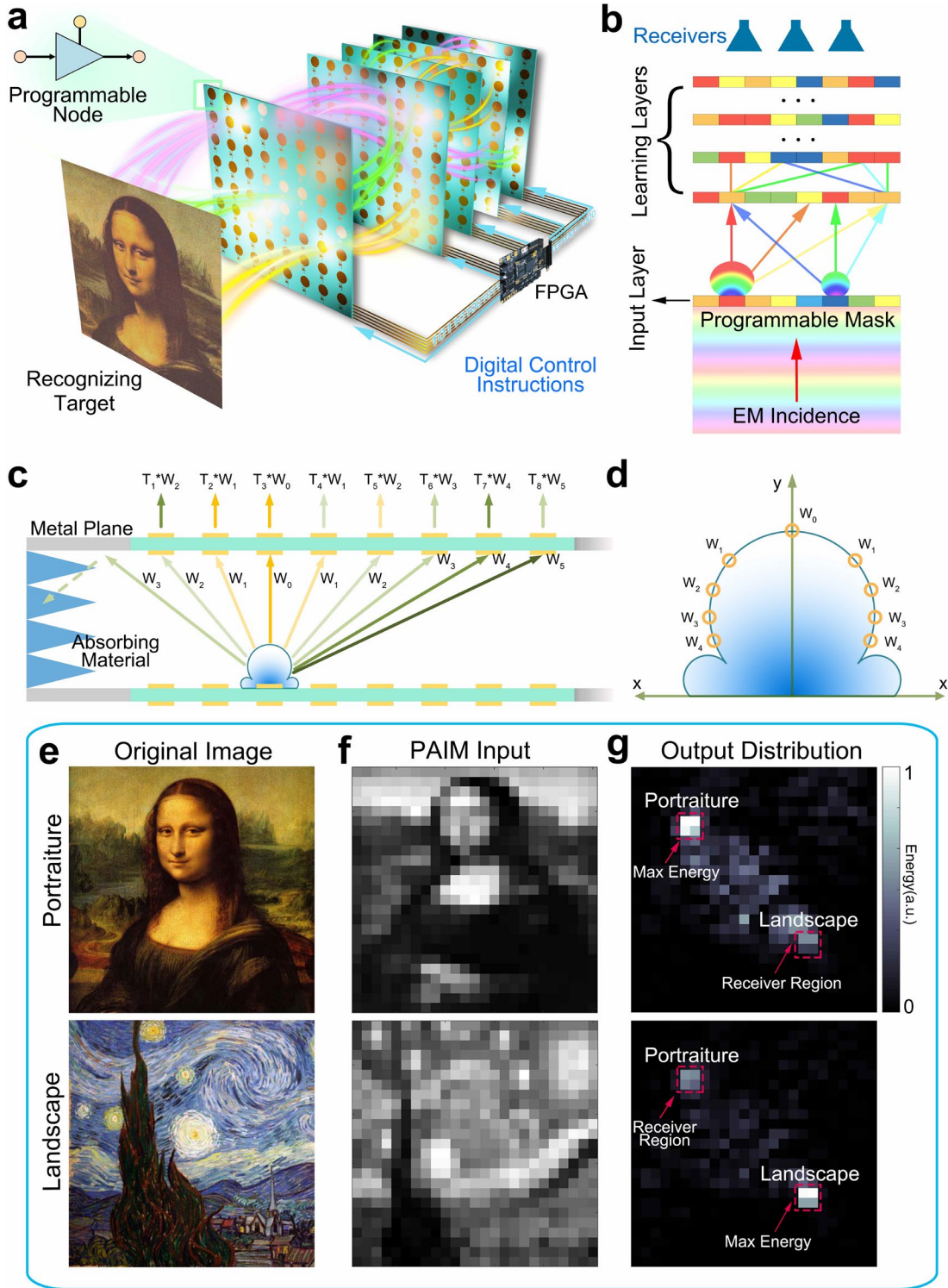


Fig. 1 | PAIM – A reprogrammable D²NN platform. **a**, An array of programmable metasurfaces is used to construct PAIM, in which several FGPAs are installed to control the gain factor of each meta-atom, making PAIM a real-time and re-trainable intelligent machine. **b**, The schematic diagram of PAIM. A meta-atom in the learning layer will receive the waves radiated from all meta-atoms in the former layer, making the PAIM structure a full-connected network. The transmission coefficient of each meta-atom can be trained by using supervised/unsupervised learning or even reinforcement learning methods to achieve various functions. The first layer acts as the input layer by using pre-set

transmission coefficients to encode the input information into the spatial distribution of EM energy.

c, The transmitted wave of a meta-atom, multiplied by propagation factors W_i , illuminates on all meta-atoms in the next layer. Then the EM wave is multiplied by the complex-valued transmission coefficient T_i to act as the secondary source of wave. **d**, The radiation pattern of a meta-atom. **e-g**,

Two testing examples for oil painting classification, in which **(e)** and **(f)** are the original pictures and their corresponding normalized visualization images of amplitude transmission coefficients in the input layer, and **(g)** illustrates the energy distributions in the output plane, demonstrating that the two pictures are successfully classified.

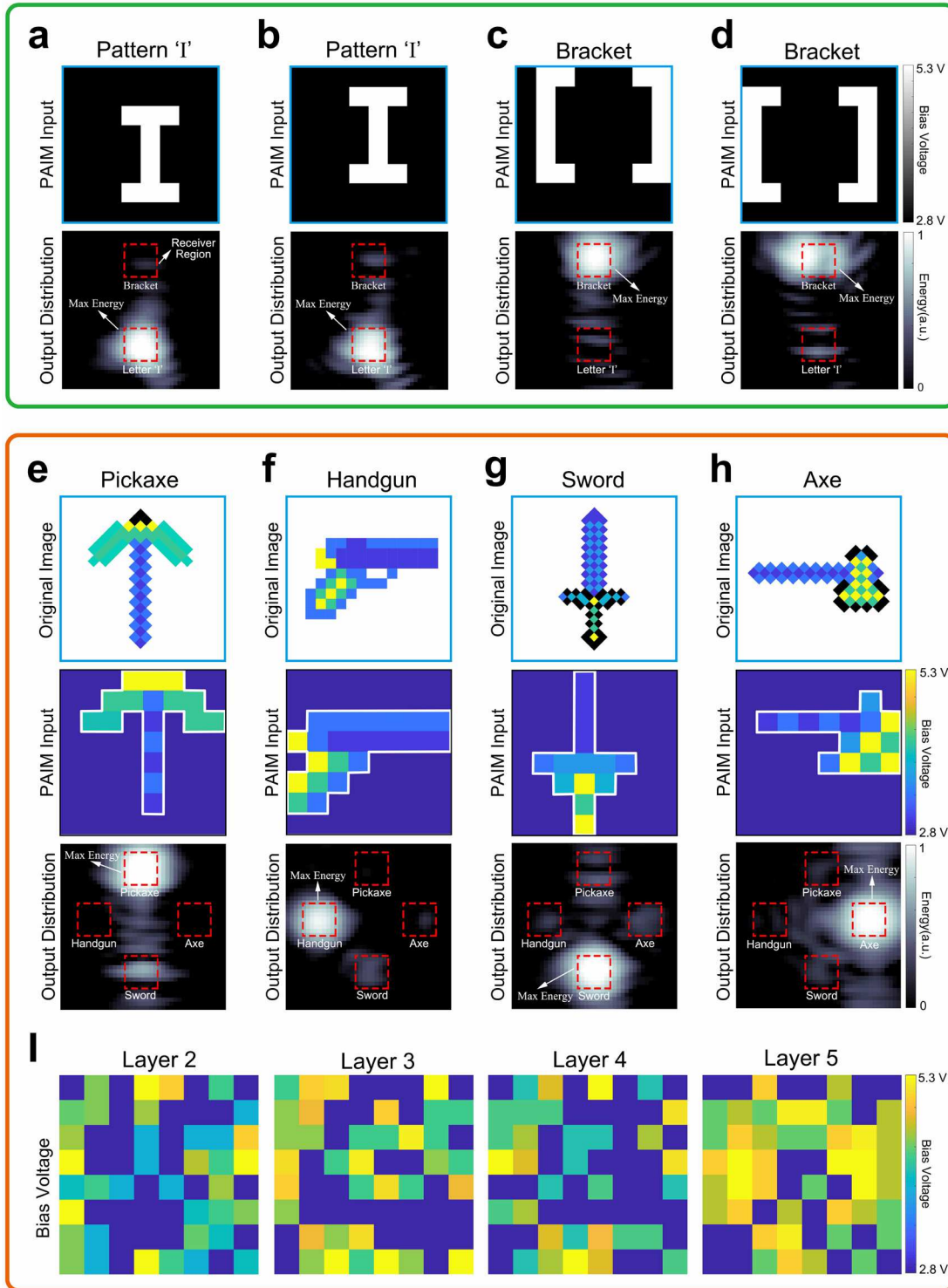


Fig. 2 | Experimental results of image classifications using PAIM. a-d, Two kinds of patterns (letter 'I' and bracket '[') are represented by the distributions of bias voltages for 8×8 meta-atoms in first PAIM layer. The input image consists of 8×8 blocky squares of colors and each square represents the bias voltage of the meta-atom. The meta-atoms in the remaining four layers are assigned the bias voltages designed from the training process and could recognize the two patterns by ranking the receiving energies from the two receiving antennas. The patterns of letter 'I' in (a) and (b) and the patterns of '[' in (c) and (d) have different locations. e-h, The original images of

game prop are down-sampled to 8×8 blocky squares of colors, representing different levels of bias voltages for 8×8 meta-atoms in first PAIM layer. The pictures of output distributions indicate the expected testing results. **i**, The bias-voltage configurations of layers 2 to 5, which are obtained by the training process running on a computer.

350

360

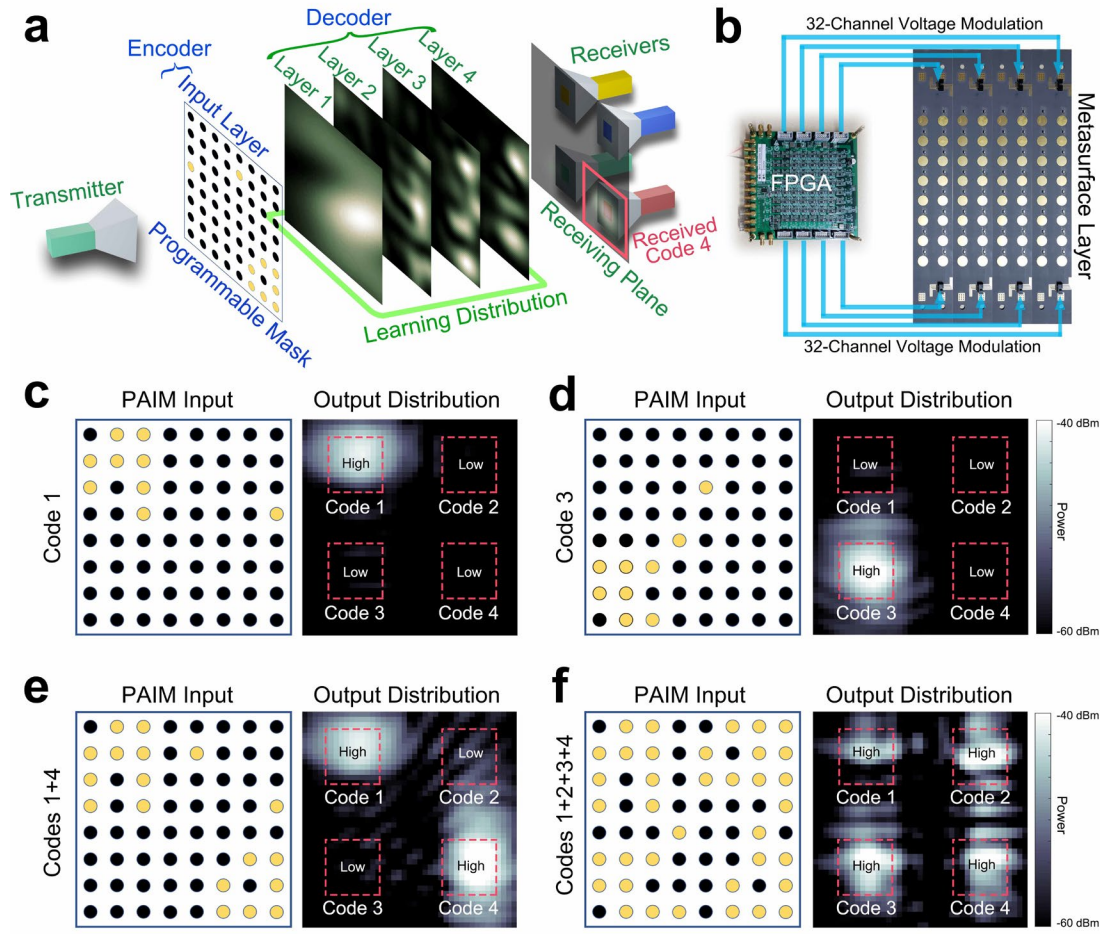


Fig. 3 | Experimental results of encoder and decoder in the CDMA task using PAIM. **a**, The energy distributions of all layers when radiating the coding information of the fourth user. The input layer acts as an encoder to transform the user code to the energy distribution in the free space. The yellow and black dots in the input layer represent the binary digits ‘1’ and ‘0’, respectively. PAIM receives the spatial energy distribution and decodes it by four metasurface layers to judge which user code has been transmitted. The input patterns of the four user codes are presented in Supplementary Fig. S11. **b**, Photograph of one of the fabricated metasurface layers, which is controlled by altogether 64-channel voltages with the corresponding FPGA. **c,d**, The energy distributions of user codes 1 and 3 on the output plane when transmitting one user code, showing that only the correct receiver corresponding to the transmitted user code could collect high energy. **e,f**, The output energy distributions when simultaneously transmitting two (1 and 4) or four (1, 2, 3, and 4) user codes. Only the receivers corresponding to the transmitted user codes collect high energies, indicating that all user codes could be decoded correctly and simultaneously.

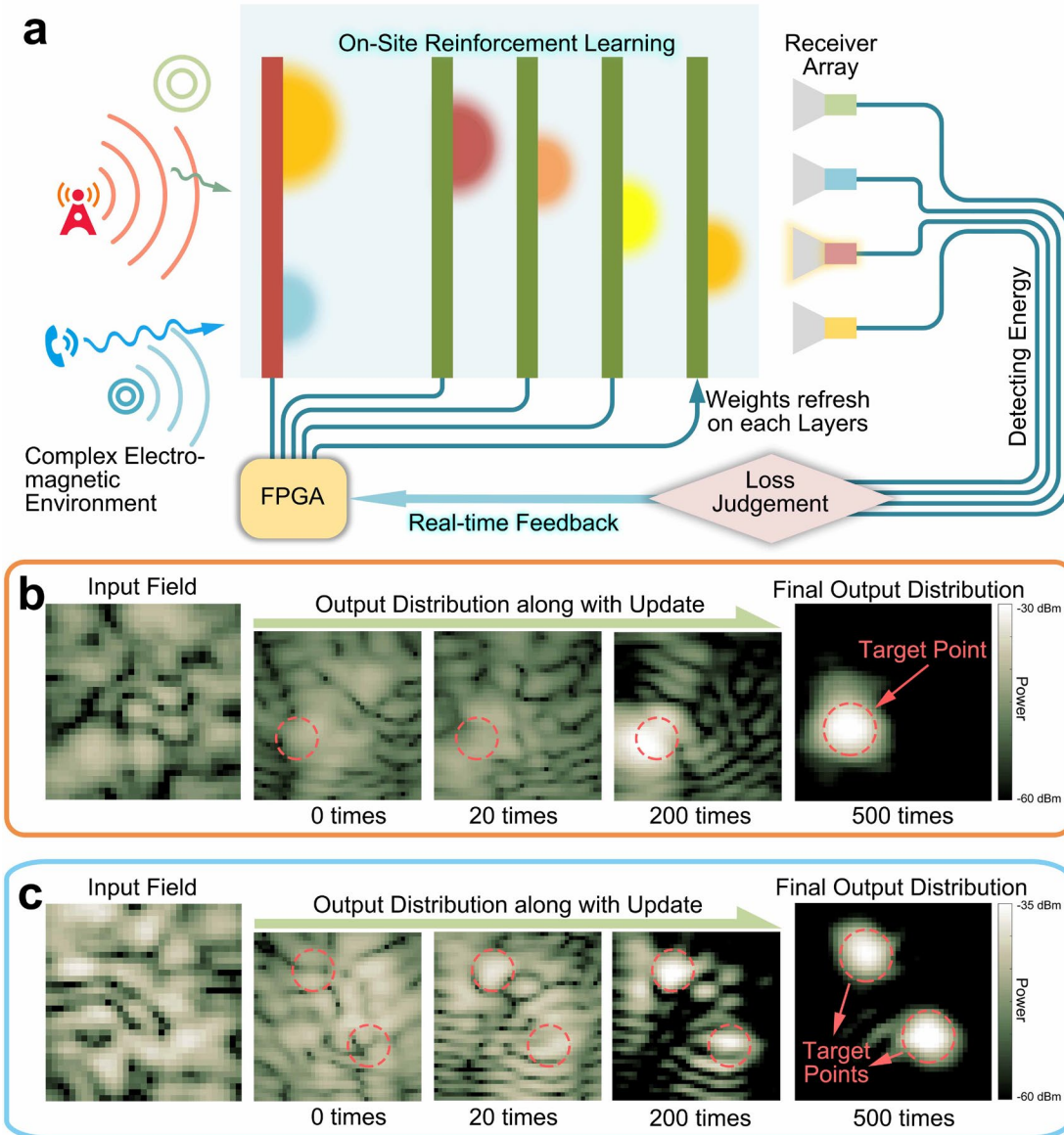


Fig. 4 | Experimental results of dynamic multi-beam focusing by the on-site reinforce-learning process using PAIM. **a**, The on-site reinforce-learning process of PAIM, in which the transmission coefficients of each PAIM layer are continually controlled by FPGA according to the real-time feedback signals. **b**, **c**, The evolution of the output energy distributions along with the updated time in the reinforce-learning process. Here, the distributions of input fields in (**b**) and (**c**) are randomly generated but remained unchanged during the reinforce-learning process. We observe that the energies of the output fields are gradually focused on the target points when the updating procedure goes on.

Supplementary Materials for

Programmable Artificial Intelligence Machine for Wave Sensing and Communications

Che Liu^{1,2, †}, Qian Ma^{1,2, †}, Zhang Jie Luo^{1,2}, Qiao Ru Hong^{1,2}, Qiang Xiao^{1,2}, Hao Chi Zhang^{1,2}, Long Miao³, Wenming Yu^{1,2,3}, Qiang Cheng^{1,2}, Lianlin Li⁴, and Tie Jun Cui^{1,2,*}

400 ¹ Institute of Electromagnetic Space, Southeast University, Nanjing 210096, China.

² State Key Laboratory of Millimeter Wave, Southeast University, Nanjing 210096, China.

³ Jiangsu Cyber-Space Science & Technology Co., Ltd., 12 Mozhou East Road, Nanjing 211111, China.

⁴ School of Electronic Engineering and Computer Sciences, Peking University, Beijing 100871, China.

*Correspondence to: tjcui@seu.edu.cn.

† Che Liu and Qian Ma: These authors contributed equally to this work.

410

420

Materials and Methods

Supplementary Note 1. FPGA Modulation and Feedback Channels of Receivers

The programmable weight matrix in PAIM is implemented with the digital voltage modulation channel from FPGA. In Fig. 3b, a voltage modulation configuration for a metasurface layer is presented, which is controlled by FPGA with 64 channels. Each channel takes charge of two amplifiers in meta-atom. The 8×8 -unit metasurface is fabricated into four detachable boards, as shown in Fig. 3b, where 64 voltage channels are divided into two bundles linking to FPGA. Each FPGA communicates with others in the network interface. Figure S1 presents the whole system configuration of the FPGA control network, where FGPA 0 is the main processor, undertaking nearly all calculation tasks and assigning the voltage control configuration to other four FPGAs (the slave processors). The receivers are connected to the last slave processing FPGA to detect the energy level on the receiving plane. The designed FPGA also equips with 16 power detection channels to distinguish the received energy.

Supplementary Note 2. Reinforce-Learning Process

To fully demonstrate the real-time re-trainable advantage of our PAIM, we specifically design a reinforce-learning task to realize dynamic multi-beam focusing. The reinforce-learning process does not need pre-prepared training data, while updates the configuration parameters according to the feedback by interacting with environment. Therefore, it could guarantee the training result to be adaptive to the actual application scenarios.

For the multi-beam focusing task, the error is calculated by the following formula:

$$Error = \sum_k y_k (s_k - \theta_k)^2 + aS^2 \quad (1)$$

where, k represents the number of points we want to concentrate the EM energy on, s_k and θ_k indicate the measured energy and desired energy at the k th point, respectively, S represents the total leaking energy, which is the sum of energies radiated outside the target point, and y_k and a are constant scale factors.

In one iteration of the training process, we randomly choose 20% trainable meta-atoms, and change their bias voltages by small random values one by one. Instantly after the bias voltage of a

450 meta-atom is changed, the change of output energy distribution is measured by the receiving antennas, and at the same time the change of error is calculated by Eq. (1), as shown in Fig. S1. If the error descends, which means that the bias voltage change of the meta-atom can make the current output EM distribution closer to the desired one, the current bias voltage will be reserved, otherwise the bias voltage will restore to the value before currently changed. In our multi-beam focusing task, PAIM could focus the electromagnetic energies to the desired positions after about 500 iterations.

One advantage of the reinforce learning is the result-oriented strategy, in which we do not need to worry about the accuracy of simulations or other factors that could make the designed parameters deviate from the measurement results. Hence, it enables PAIM to deal with very complicated and unknown environments, broadening the application range of PAIM.

460

Supplementary Note 3. Forward Propagation Model.

Figure 1b demonstrates the 2D structure of the PAIM model, and a more detailed version is illustrated in Fig. S2. We use $\mathbf{E}^i, i = 0, 1, 2, \dots, M$ to represent the complex electric field illuminating on the i -th PAIM layer, which is an N -dimensional vector (N is the number of meta-atoms in a layer), and each element indicates the field received by the corresponding meta-atom. \mathbf{E}^{M+1} is the complex field on the output plane (output layer). Thus, the length of \mathbf{E}^{M+1} depends on the number of receiving antennas or the sampling numbers of moving probe. $\mathbf{T}^i, i = 0, 1, 2, \dots, M$ represents the complex transmission coefficients of the i -th layer, which is also an N -dimensional vector and each element in this vector corresponds to the complex transmission coefficient of each meta-atom in the i -th layer. Then the forward propagation formula can be written as:

470

$$\mathbf{E}^{i+1} = \mathbf{W}^i (\mathbf{E}^i \odot \mathbf{T}^i), i = 0, 1, 2, \dots, M \quad (2)$$

in which \odot is the Hadamard product and \mathbf{W}^i represents the space attenuation coefficients from the i -th layer to the $(i+1)$ -th layer. In fact, $\mathbf{W}^i, i = 0, 1, 2, \dots, M-1$ is an $N \times N$ dimensional matrix, and its element in the p -th row and q -th column represents the space attenuation coefficient from the q -th meta-atom in the i -th layer to the p -th meta-atom in the $(i+1)$ -th layer. \mathbf{W}^M connects the last PAIM layer and the output layer, and hence it is a $K \times N$ matrix and K is the number of receiving antennas or the sampling number of moving probe. The schematic diagram of EM-wave propagations between

adjacent layers and the radiation pattern of one meta-atom are demonstrated in Fig. 1c, d. The symbols $W_n, n = 1, 2, 3, 4, \dots$ in Fig. 1d are different from the matrix \mathbf{W}^i in Eq. (2). In fact, $W_n, n = 1, 2, 3, 4, \dots$ constitute one of the columns in \mathbf{W}^i . Using the hierarchical formula (2), we get the final output field (\mathbf{E}^{M+1}), once the input field (\mathbf{E}^0) is given.

Supplementary Note 4. Error Backpropagation.

Eq. (2) presents the forward propagation model of PAIM, which is a linear model. We use \mathbf{a}^i and Φ^i to represent the amplitude and phase parts of $\mathbf{T}^i, i = 0, 1, 2, \dots, M$, respectively. The gradients of \mathbf{a}^{M-L} and $\Phi^{M-L}, L = 0, 1, 2, \dots, M$ can be easily obtained by matrix multiply operations using the chain rule of derivative:

$$\begin{aligned} \frac{\partial \mathbf{E}^{M+1}}{\partial \Phi^{M-L}} &= \frac{\partial \mathbf{E}^{M+1}}{\partial \mathbf{T}^{M-L}} \frac{\partial \mathbf{T}^{M-L}}{\partial \Phi^{M-L}} = \mathbf{A}^{M-L} \text{diag}(j\mathbf{T}^{M-L}) \\ \frac{\partial \mathbf{E}^{M+1}}{\partial \mathbf{a}^{M-L}} &= \frac{\partial \mathbf{E}^{M+1}}{\partial \mathbf{T}^{M-L}} \frac{\partial \mathbf{T}^{M-L}}{\partial \mathbf{a}^{M-L}} = \mathbf{A}^{M-L} \text{diag}(\exp(j\Phi^{M-L})) \\ \mathbf{A}^{M-L} &= \mathbf{W}^M \text{diag}(\mathbf{T}^M) \mathbf{W}^{M-1} \text{diag}(\mathbf{T}^{M-1}) \mathbf{W}^{M-2} \text{diag}(\mathbf{T}^{M-2}) \dots \mathbf{W}^{M-L} \text{diag}(\mathbf{E}^{M-L}) \end{aligned} \quad (3)$$

The matrix partial derivatives in Eq. (3) apply for the numerator format and *diag* means matrix diagonalization. For different tasks, we define different error functions, symbolized by $\text{Error}(\mathbf{E}^{M+1})$. For the classification tasks, we use cross entropy error function; and for other tasks, we use mean square error function. Applying the chain rule, the final gradient formula can be written as:

$$\begin{aligned} \frac{\partial \text{Error}(\mathbf{E}^{M+1})}{\partial \mathbf{a}^{M-L}} &= \frac{\partial \text{Error}(\mathbf{E}^{M+1})}{\partial \mathbf{E}^{M+1}} \frac{\partial \mathbf{E}^{M+1}}{\partial \mathbf{a}^{M-L}} \\ \frac{\partial \text{Error}(\mathbf{E}^{M+1})}{\partial \Phi^{M-L}} &= \frac{\partial \text{Error}(\mathbf{E}^{M+1})}{\partial \mathbf{E}^{M+1}} \frac{\partial \mathbf{E}^{M+1}}{\partial \Phi^{M-L}} \end{aligned} \quad (4)$$

When all gradients are calculated, the method of gradient descent is used to optimize \mathbf{a}^i or Φ^i independently or simultaneously. Various kinds of deep learning optimizers can be used, such as Adam³⁹.

Supplementary Note 5. Simulation Classification Tasks.

The most classical deep learning task is image classification, among which the handwritten digit recognition is one of the most canonical tasks. We firstly simulate PAIM to deal with the handwritten digit recognition task. After training with 60,000 handwritten digit images and testing with 10,000 images (MNIST dataset), the mean accurate rate of recognizing 10 digits is 90.76%, and some results are shown in Fig. S3.

In order to fully demonstrate the advantages of PAIM, we also simulate the oil painting style classification task to show the real-time adjustable character of the input layer and trainable layers in PAIM. This task also proves that PAIM can possess some part of high-level human intelligence like art appreciation. In this task, the oil paintings are classified as portraiture or landscape paintings. After training with 500 oil paintings and testing with 100 paintings, PAIM can reach a classification accuracy of 97%. Some testing results are shown in Fig 1e-g, and Fig. S4.

Supplementary Note 6. Meta-Atom Structure and its Modulation Performance.

The PAIM architecture requires that the information metasurface has the capability to control transmitted waves with different gain levels in programmable way. Hence the meta-atom must include the amplifier devices. The optimized meta-atom is illustrated in Fig. S5a, comprising of a transmission-type meta-structure and two high-efficiency amplifier chips. Each meta-atom is a programmable node for modulating the incident wave, by implementing specific voltages on the amplifier chips. The detailed modulation mechanism of the meta-atom is shown in Fig. S5b, where the transmission energy is firstly coupled into the top circular patch for the amplitude modulation. Then the energy is amplified twice within the two amplifiers, between which a via-hole is placed to connect the top and bottom structures.

The meta-atom is composed of three substrate layers: two F4B layers (with 1 mm thickness) and a prepreg layer (with 0.2 mm thickness) between the F4B layers. Figure S5c shows the front view of the presented meta-atom, where the detailed parameters are given by $a=40$ mm, $b=20.76$ mm, $c=15.2$ mm, $d=3.84$ mm, and $e=6.2$ mm. A symmetrical structure is arranged on the bottom view. The integrated circuit module is marked with a blue rectangle, whose circuit components are further exhibited in Fig. S5d. Ports 1 and 2 in the module are connected to the circular patch and via-hole, respectively. A commercial amplifier chip (Qorvo TQP369180) is applied, whose amplifying level can be regulated by applying different supplying voltages. The designed values of the components in Fig.

S5d are given as: $C1=18\text{ nF}$, $C2=1\text{ nF}$, $C3=1\text{ uF}$, $C4=56\text{ pF}$, $C5=56\text{ pF}$, $R1=24\text{ }\Omega$, and $L1=39\text{ nH}$.

530

To clearly present the modulation performance of the meta-atom, we firstly examine its amplitude-modulation range. Figure S6a illustrates the experimental configuration for the transmission amplitude test within a vector network analyzer (VNA). One element in the central region is activated by a DC power supply, as shown in Fig. S6b, which is exactly facing the lens antenna. It should be noted that all other elements are power-off, which could be considered as perfect isolator. Thus, the energy from the transmitter can almost only go through the activated element. In Fig. S6c, the measured results of the meta-element from 4.5 to 6.5 GHz are marked in different colors and line styles when distinct voltages are applied from 2.9 to 5V. In these results, we clearly observe that the transmission amplitude changes from -35 dB to -5 dB in its working band from 5.35 to 5.7 GHz. To exhibit the relationship between the supplying voltage and amplitude modulation, we provide an altering plot at 5.64 GHz as the voltage changes from 2 to 5 V, as presented in Fig. S6d. We notice that the total range of transmission coefficient covers about 35 dB (from -40 dB to -5 dB), in which a sharp transformation occurs at the voltage of 3.8 V. We remark that the transmission amplitude of air window (with the same dimension of meta-atom) is -18 dB. Thus, the applied element can realize the transmission energy reduction (down to -22 dB) and amplification (up to 13 dB), promising the enough manipulation range for the weight matrix.

540

Supplementary Note 7. Supporting Structure Configuration for PAIM.

In the experiments, PAIM is fixed into a fully-covered supporter, as shown in Fig. S7a. Five metasurface layers with an interval of 10cm are settled on a metal structure, fabricated from aluminum alloy. Each metasurface layer is screwed on a metal board with $560 \times 560\text{ mm}^2$, to prevent unnecessary diffractions among layers. The whole metal structure is covered with microwave absorbing material on the surrounding, to further reduce the undesired diffraction and scattering. The receiving plane is set at 100mm away from the last metasurface layer, as presented in green color. FPGA for each metasurface layer is screwed on the metal board, out of the covering of the microwave absorbing materials, to reduce the interference from anomalous scattering by FPGA. In the nearly-closed system, the energy emitted by the meta-atoms on the learning layers can hardly influence its input since the amplifiers only allow unidirectional transmissions, which greatly suppresses the self-exciting

550

oscillations. The front view and side view of the structure are provided in Fig. S7b, c.

560 **Supplementary Note 8. Experimental Setup.**

The testing system is shown in Fig. S8, in which PAIM is packaged with wave-absorbing materials to reduce the influence from environmental noise and edge diffraction. The energy distribution measurement is performed by near-field microwave test in a standard chamber room, as exhibited in Fig. S8c, d. The whole PAIM is placed on a test platform, with a horn antenna for initial excitation. A waveguide detector in C band is applied as the near-field probe for measurement, and a vector network analyzer is used to measure the amplitudes and phases of EM waves. The measured plane (the receiving plane) is set at 100 mm away from the last-layer metasurface, as shown in Fig. S8d.

Supplementary Note 9. Discrete Optimization Algorithm.

570 In practice, the complex transmission coefficient of meta-atom cannot be controlled continuously, which can only be set by several discrete values. Thus, it is necessary to develop a *discrete optimization algorithm* to optimize the complex transmission coefficients of the meta-atom. The aim of the discrete optimization algorithm is the same as the aforementioned gradient descent optimization algorithm: minimizing the error function. We use $a_p^i, i=1,2,...,M; p=1,2,...,N$ to present the complex transmission coefficient of the p -th meta-atom in the i -th layer, whose complex transmission coefficients are represented as \mathbf{T}^i . The procedure of the optimization algorithm is given as follows (optimizing a_p^i as example).

- **Step 1:** Initialize all parameters of $\mathbf{T}^i, i=0,1,2,...,M$ by discretizing the uniform random distribution.
- 580 ● **Step 2:** Calculate the output electric fields (\mathbf{E}^{M+1}) by using the forward propagation formula (2) and the current error $Error_0 = Error(\mathbf{E}^{M+1})$ by the self-defined error function.
- **Step 3:** Initialize the update step value of a_p^i randomly, which is expressed by Δd_p^i . Δd_p^i is usually the difference of adjacent discrete values. Because the linearity of our network, if the value

of a_p^i increases by Δd_p^i , the output field will increase by $\Delta d_p^i \cdot \frac{\partial \mathbf{E}^{M+1}}{\partial a_p^i}$. Thus, the output field

becomes $\mathbf{E}^{M+1} + \Delta d_p^i \cdot \frac{\partial \mathbf{E}^{M+1}}{\partial a_p^i}$. Calculate the auxiliary error by

$$Error_p^i = Error(\mathbf{E}^{M+1} + \Delta d_p^i \cdot \frac{\partial \mathbf{E}^{M+1}}{\partial a_p^i}) \quad (5)$$

- **Step 4:** Compare the values of $Error_0$ and $Error_p^i$. If $Error_0 \leq Error_p^i$, the value of a_p^i remains unchanged; otherwise, the value of a_p^i is updated and replaced by $a_p^i + \Delta d_p^i$.

For all $a_p^i, i = 1, 2, \dots, M; p = 1, 2, \dots, N$, we execute Step 2 to Step 4 in loops until the current error is less than the pre-set value, and then save the corresponding $\mathbf{T}^i, i = 0, 1, 2, \dots, M$ as the final optimization outcome. Several methods could be used to accelerate the optimization process, such as organizing the computational process in matrix form or using parallel algorithms.

Supplementary Note 10. Experimental Classification Tasks.

The aforementioned simulation tasks verify the flexibility and feasibility of the deep learning structure of PAIM. Next, we design a pattern recognition task and test it by our manufactured PAIM. We design two kinds of patterns: letter ‘I’ and bracket ‘[]’ (see Fig. S9). The meta-atoms consisting of such patterns on the input layer are given a high bias voltage, and the background meta-atoms are set as relatively low voltage. To expand the variety of the input data, besides moving the location of patterns, we add some white Gaussian noises, i.e., the voltages of meta-atoms are added by a random deviation with small disturbance in both training and testing process. After training, such two kinds of patterns can be recognized with an accuracy of 100% in 200 trials. More testing results are given in Fig. S9.

The aim of designing the game props recognition is to display the richness of input forms of our PAIM. Benefit from the adjustable bias voltages of meta-atoms, we could input colorful images by scaling different colors on different bias voltages. The comparison between simulation and experimental results in this case is shown in Fig. S10, in which we find that there are some differences between low energy regions in the simulated and measured distributions. This may be caused by the pose difference of the transmitting horn antenna, weak diffraction from edges of aluminum alloy

support, and coupling effect among meta-atoms. However, such differences have little effect on
610 designing our parameters because only the high-energy distribution regions have more impacts.

Supplementary Note 11. Comparison of Codec Tasks between the Traditional and Presented Methods.

In the mobile communication codec task, we design four kinds of orthogonal codes, each of which is a string of binary numbers with length of 64. We reshape the 64-dimensional coding vectors into 8×8 matrices so that they could be represented by our input layer, which has 8×8 meta-atoms. After reshaping, the four kinds of codes are shown in Fig. S11. By using PAIM, they could be encoded and decoded independently even when they are transmitted in the same information channel simultaneously (Fig. S11).

620 In the traditional Code Division Multiple Access (CDMA), the time consumption to send a message bit is proportional to the length of encoding (Fig. S12a), which is 64 in our cases. Different from the traditional CDMA, our PAIM could take the space-for-time strategy to spread the codes into space distribution, and thus the time consumption of sending a message is very tiny and has a fixed value (Fig. S12b). This property is very useful in short-distance wireless communications with high channel capacity and low time delay. Meanwhile, the parameters of PAIM could be regarded as a natural encryption key, and hence our system has native encrypted communication ability. The communication distance could be increased by enlarging the size of the input PAIM layer or using other transmission strategies.

630 Supplementary Note 12. Further Decoding Function of PAIM for Communication.

The transmission distance between encoder and decoder is 32cm in the current system, which is mainly restricted by the encoder layer of PAIM. The limited number of meta-atoms and the relatively short interval between two meta-atoms restrict the generation of variegated EM field distributions for a long transmission distance, increasing the difficulty to distinguish the distributions from different combinations of user codes.

Luckily, the decoding function of PAIM is independent of the encoder layer, and thus the transmission distance could be extremely increased by using other radiated strategies like the distributed transmitting antennas and reflected coding metasurfaces (Fig. S13). These radiated

strategies could generate distinguishable EM field distributions at the position of PAIM, and other
640 novel methods to encode different user codes could be explored to transmit the binary information.
Also, the space-for-time strategy could be used to reduce the time delay.

Besides the space-for-time strategy, our PAIM uses EM waves to do calculations, making the
decoding process be executed at the speed of light, further reducing the time delay in mobile
communications. With the development of the fifth or sixth generation of communications, the
increase of channel capacity becomes more important and space division multiplexing technique has
attracted more attention. PAIM offers a new idea to fully explore the space distribution of EM waves
and realize the space division multiplexing.

Supplementary Note 13. Calibration of the Space Attenuation Coefficients.

650 As shown in Fig. 1d, the space attenuation coefficients \mathbf{W}^i in Eq. (2) could be obtained by measuring
the EM field distribution of a meta-atom on the output plane. Owing to the inconsistency of meta-
atoms arising in fabrication and the small deformation during assembling process of PAIM, however,
the value of \mathbf{W}^i will deviate from the initial one, which would bring difficulties to parameter designs
in the training process. Thus, we need to calibrate the value of \mathbf{W}^i before starting the training process.

Firstly, we acquire 5000 experimental samples. For each sample, we randomly set the bias
voltages on all meta-atoms in PAIM and measure the output field distributions by a specially designed
8×8 receiving antennas array. We remark that the number of experimental samples should not be small,
otherwise the parameters will over fit the data set and reduce the accuracy of simulations. Secondly,
we use gradient descent method to correct the value of \mathbf{W}^i . Before introducing the detailed approach,
660 we need to define some symbols. The definitions of \mathbf{E}^i , \mathbf{T}^i and $\mathbf{W}^i, i = 0, 1, 2, \dots, M$ are the same as
those in Eq. (2) and \mathbf{E}^{M+1} represents the calculated complex field value on the output plane when \mathbf{E}^0
and $\mathbf{T}^i, i = 0, 1, 2, \dots, M$ are given. Here, \mathbf{E}^0 is obtained by measuring the EM fields from the
transmitting antenna and $\mathbf{T}^i, i = 0, 1, 2, \dots, M$ is set according to the bias voltage of each meta-atom at
the i -th layer. We use $\tilde{\mathbf{E}}^{M+1}$ to represent the output fields obtained by real measurements. Then, the
error function for the gradient descent method is written as

$$Error = \left| \tilde{\mathbf{E}}^{M+1} - \mathbf{E}^{M+1} \right|^2 \quad (6)$$

Since the error function is not an analytical function, we need to calculate the gradients to the amplitude and phase parts of \mathbf{W}^i respectively. We use matrix $\boldsymbol{\rho}^i$ and $\boldsymbol{\phi}^i, i=0,1,2,\dots,M$ to denote the amplitude and phase parts of \mathbf{W}^i : $\mathbf{W}^i = \boldsymbol{\rho}^i \odot \exp(j\boldsymbol{\phi}^i)$, in which \odot represents the Hadamard product, and j means the unit imaginary number. We choose \mathbf{W}^i as the trainable parameters, and the calibration process is described as follows.

- **Step 1:** Initialize $\mathbf{W}^i, i=0,1,2,\dots,M$ using the values obtained from the field distribution of a meta-atom according to the definition of \mathbf{W}^i .
- **Step 2:** Choose one sample in the 5000 experimental samples, set the values of $\mathbf{T}^i, i=0,1,2,\dots,M$ according to the bias voltages of meta-atoms, and calculate the value of \mathbf{E}^{M+1} using Eq. (2).
- **Step 3:** Calculate the gradients of error to $\boldsymbol{\rho}^{M-L}$ and $\boldsymbol{\phi}^{M-L}, L=1,2,\dots,M$ respectively:

$$\frac{\partial Error}{\partial \boldsymbol{\rho}^{M-L}} = 2\text{Real} \left[\left(\mathbf{A}^{M-L} \right)^T \left(\mathbf{E}^{M+1} - \tilde{\mathbf{E}}^{M+1} \right)^* \left(\mathbf{B}^{M-L} \right)^T \odot \exp(j\boldsymbol{\phi}^{M-L}) \right] \quad (7)$$

$$\frac{\partial Error}{\partial \boldsymbol{\phi}^{M-L}} = 2\text{Real} \left[\left(\mathbf{A}^{M-L} \right)^T \left(\mathbf{E}^{M+1} - \tilde{\mathbf{E}}^{M+1} \right)^* \left(\mathbf{B}^{M-L} \right)^T \odot (j\mathbf{W}^{M-L}) \right] \quad (8)$$

in which, $*$ means the complex conjugate transpose; \mathbf{A}^{M-L} and \mathbf{B}^{M-L} are calculated by

$$\mathbf{A}^{M-L} = \mathbf{W}^M \text{diag}(\mathbf{T}^M) \mathbf{W}^{M-1} \text{diag}(\mathbf{T}^{M-1}) \mathbf{W}^{M-2} \text{diag}(\mathbf{T}^{M-2}) \dots \mathbf{W}^{M-L+1} \text{diag}(\mathbf{T}^{M-L+1}) \quad (9)$$

$$\mathbf{B}^{M-L} = \text{diag}(\mathbf{E}^{M-L}) \mathbf{T}^{M-L} \quad (10)$$

For $\boldsymbol{\rho}^M$ and $\boldsymbol{\phi}^M (L=0)$, we have

$$\frac{\partial Error}{\partial \boldsymbol{\rho}^M} = 2\text{Real} \left[\left(\mathbf{E}^{M+1} - \tilde{\mathbf{E}}^{M+1} \right)^* \left(\mathbf{B}^M \right)^T \odot \exp(j\boldsymbol{\phi}^M) \right] \quad (11)$$

$$\frac{\partial Error}{\partial \boldsymbol{\phi}^M} = 2\text{Real} \left[\left(\mathbf{E}^{M+1} - \tilde{\mathbf{E}}^{M+1} \right)^* \left(\mathbf{B}^M \right)^T \odot (j\mathbf{W}^M) \right] \quad (12)$$

- **Step 4:** Calibrate the value of \mathbf{W}^i by calibrating $\boldsymbol{\rho}^i$ and $\boldsymbol{\phi}^i, i=0,1,2,\dots,M$ respectively

$$\boldsymbol{\rho}_{(2)}^i = \boldsymbol{\rho}^i - l * \frac{\partial Error}{\partial \boldsymbol{\rho}^i} \quad (13)$$

$$\mathbf{a}_{(2)}^i = \mathbf{a}^i - l * \frac{\partial Error}{\partial \mathbf{a}^i} \quad (14)$$

in which, l indicates the learning rate for updating, and could be set an initial value as $3e^{-4}$. The learning rate needs to be gradually decreased during the calibration process.

- 690 ● **Step 5:** Execute Step 2 to Step 4 in loops until the current error is less than the pre-set value or reaches the maximum number of iterations, then output $\mathbf{W}^i, i = 0, 1, 2, \dots, M$ as the calibration results.

The comparison between the measured and simulated energy distributions after the calibration is shown in Fig. S14. We observe that the high energy regions in measured and simulated field distributions agree very well with each other.

Supplementary Note 14. Improving the Accuracy of Simulations.

The accuracy of simulation is very important, since it directly impacts the accuracy of training process for designing the bias voltage values of meta-atoms. The main factors that influence the simulation accuracy include inconsistency of meta-atoms, deformation of the PAIM's support structure, error of bias voltages, and coupling effect among adjacent meta-atoms.

The inconsistency of meta-atoms could give rise to slight deformation of radiation pattern of each meta-atom, and mainly influence the amplitude part of the space attenuation coefficients \mathbf{W}^i in Eq. (2). It is caused in the manufacturing process of PAIM. Certainly, we could measure the radiation patterns of all meta-atoms to calibrate the effect of inconsistency. However, it is too slow and laborious, and has little improvement to the simulation accuracy. The deformation of the PAIM's support structure is mainly caused by the assembly error and bending of metasurface caused by squeezing the wave-absorbing materials. It mainly influences the phase part of the space attenuation coefficients \mathbf{W}^i in Eq. (2). Thus, by the aforementioned calibration process of the space attenuation coefficients, we could reduce the influence caused by both inconsistency of meta-atoms and deformation of the support structure.

The error of bias voltages is mainly caused by the circuitry and will bring tiny error between the actual bias voltage and designed bias voltage of each meta-atom. The influence of this error could be reduced by enlarging the distance between two nearest bias voltage values.

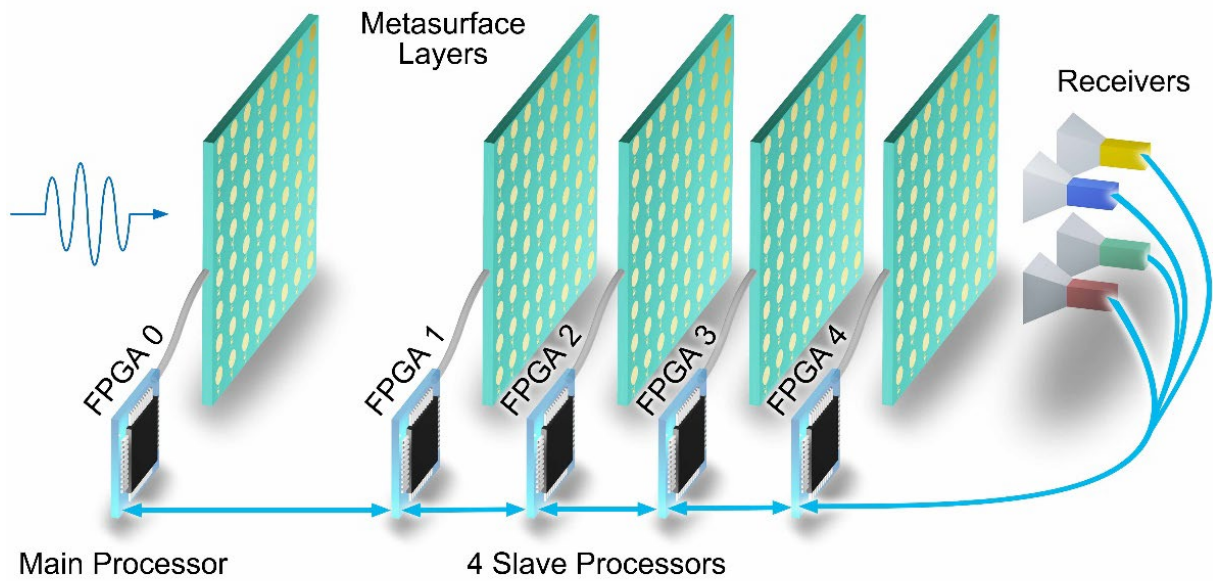
The coupling effect among adjacent meta-atoms is caused by the interaction among adjacent meta-atoms and the reflected waves from the front metasurface. It is the most intractable factor to cause the difference between the simulated and measured distributions. The coupling effect cannot be eliminated by the calibration process of the space attenuation coefficients, because it is a nonlinear interaction. However, during experiments, we find that increasing the sparsity of bias voltages could reduce the effect of coupling. Hence, we try to reduce the number of large bias voltage parameters and increase the number of low bias voltage parameters. We achieve this purpose by adding a 1-Norm Error (sum of absolute difference) to the loss function in the training process

$$L_1 = a \sum_i \|\mathbf{T}^i\|_1 \quad (15)$$

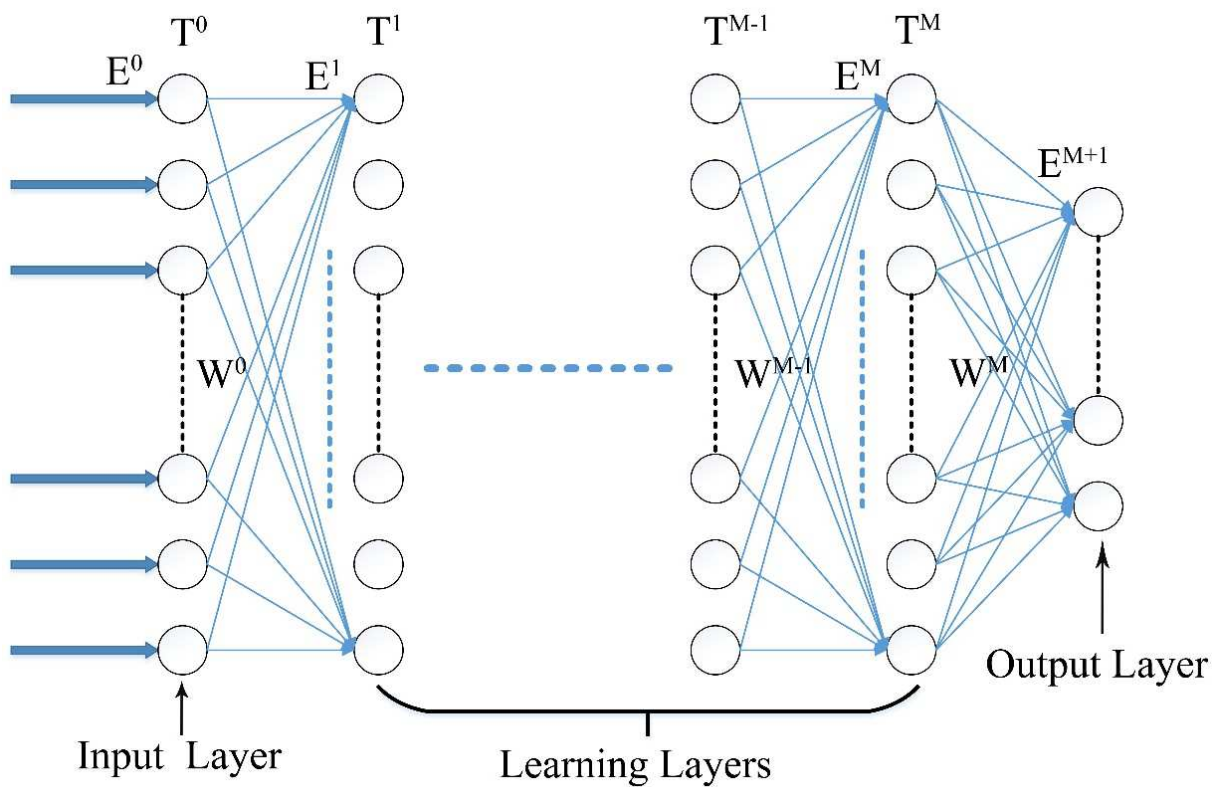
in which a is a scale factor and $\|\cdot\|_1$ is the 1-Norm function. The participation of the 1-Norm Error will make the complex transmission coefficients \mathbf{T}^i be sparser and thus reduce the influence of coupling effect. In addition, it has an extra benefit to prevent the EM energy to exceed the power transfer limit of meta-atoms by reducing the high bias voltages. Furthermore, the sparsity of parameters could increase the generalization ability of our system⁴⁰.

Lastly, an extra influence needs to mention: the pose change of transmitting horn antenna. In theory, the relative position between PAIM and transmitting antenna should remain unchanged during the whole experiment process. However, because of the accidental touch or other factors, the pose or position of the horn antenna may be different for two separate experiments. Luckily, we found that the small offset of transmitting horn antenna has little influence on the energy distribution of outputs, but may influence the phase distribution. The phase distribution on the outputs is important for the aforementioned calibration process. Hence, we need to guarantee that the position of transmitting horn antenna remains unchanged during acquisition of training data to calibrate the space attenuation coefficients. Once the space attenuation coefficients are calibrated, the effect of small offset of the transmitting horn antenna could be neglected.

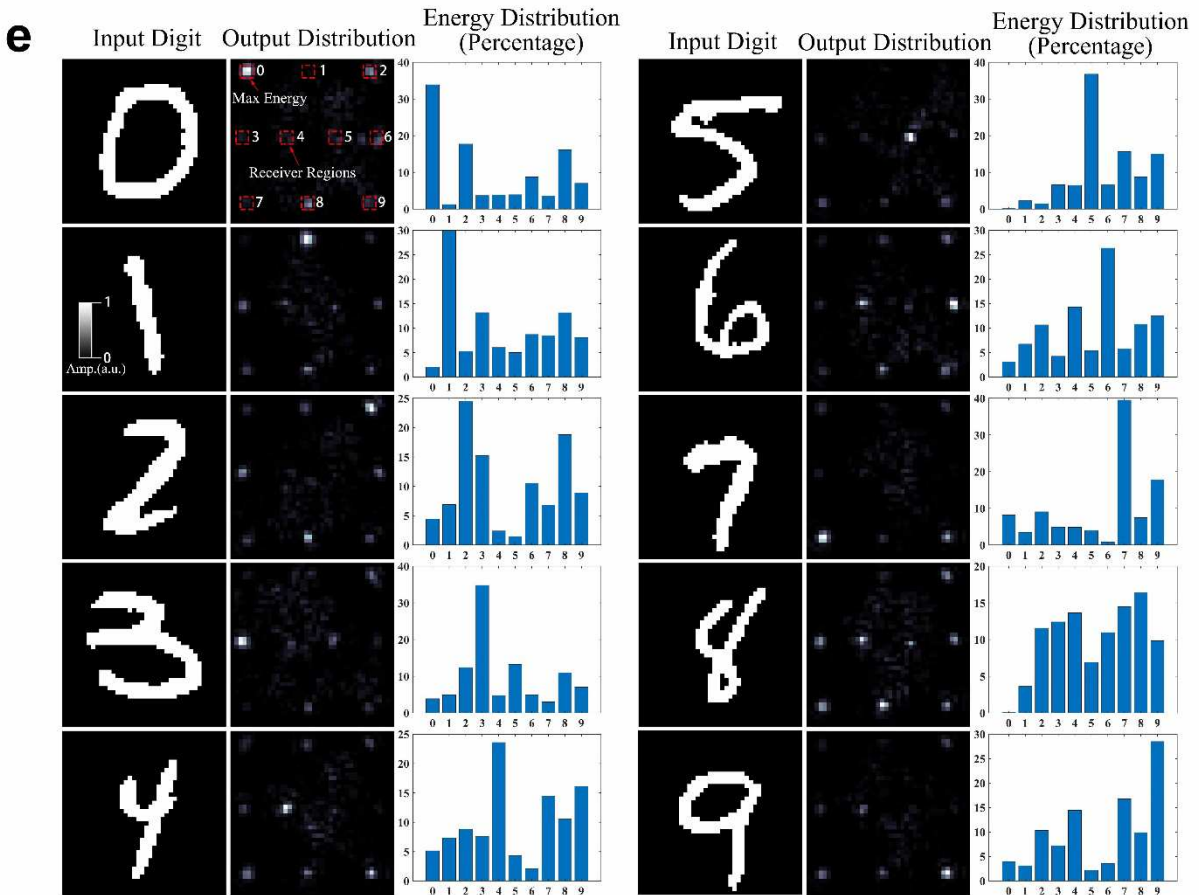
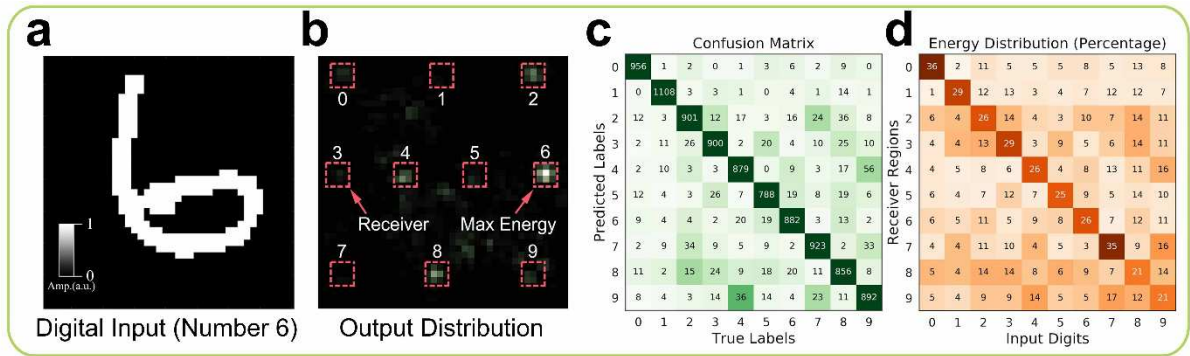
Supplementary Figures



Supplementary Figure S1 | The assembled FPGA modulation network for PAIM. The receiving antenna array would get the field distribution of EM waves, which is processed by FPGAs. FPGAs also guide the update of bias voltages of meta-atoms.

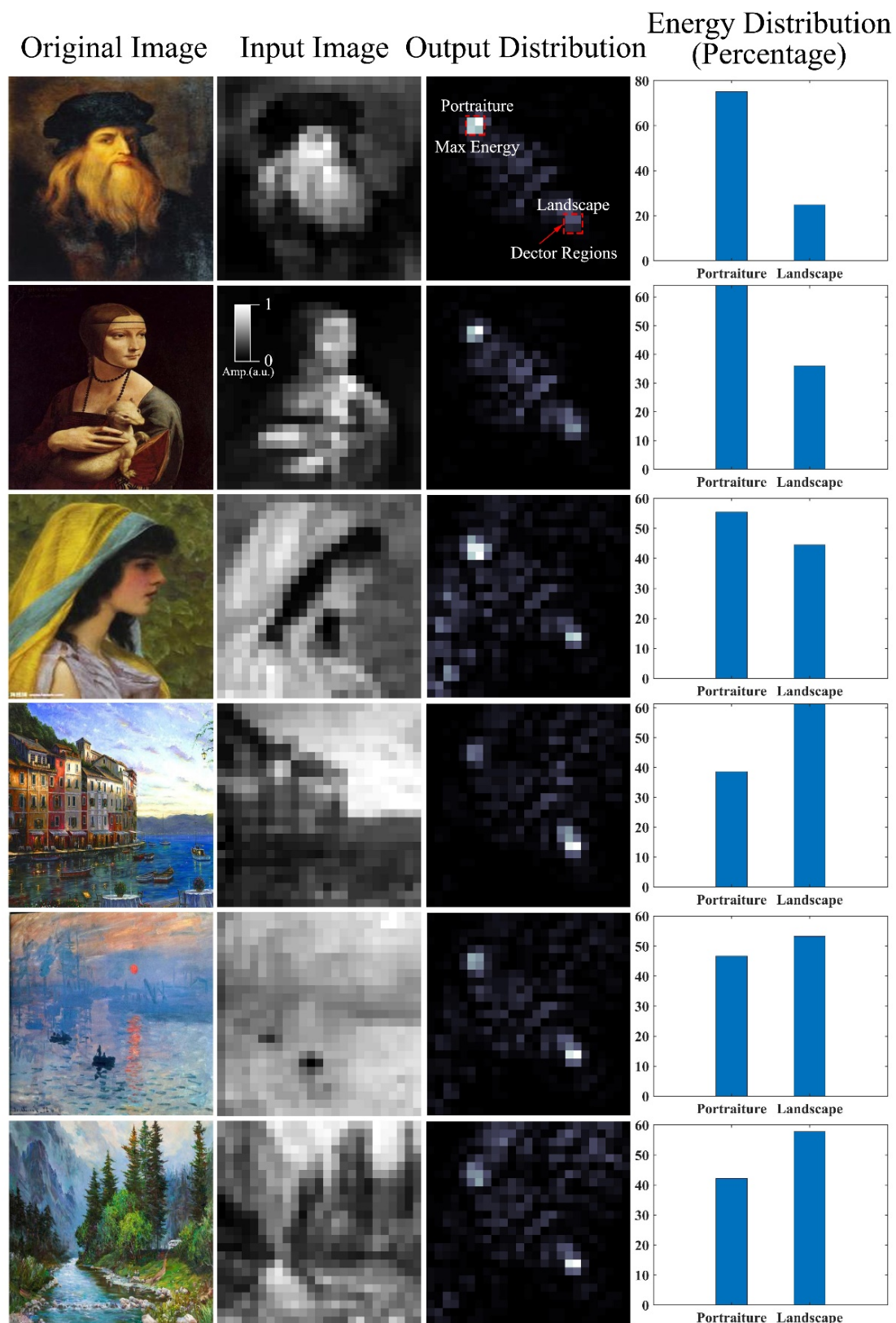


Supplementary Figure S2 | 2D structure of the PAIM model. The circles represent the meta-atoms, whose transmission coefficients constitute the trainable part of PAIM. The EM field can be amplified or attenuated by the meta-atom and transmitted to all meta-atoms in the next layer. Hence, our PAIM is a fully connected complex-value network.

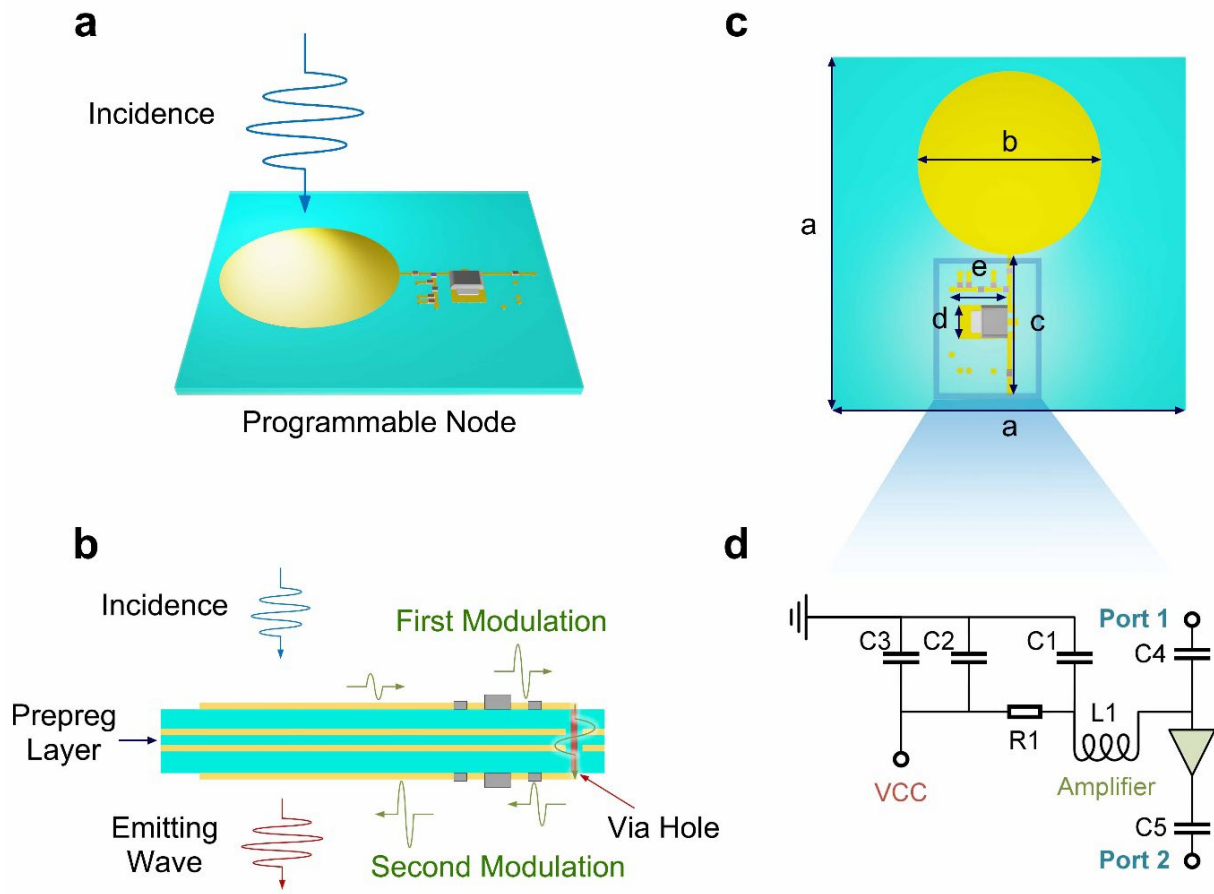


Supplementary Figure S3 | The simulation results for handwritten digit recognition. a-d, The simulated results of PAIM to deal with the classification task of handwritten digits. The first PAIM layer is used as the digital input layer, and 10 different receivers are placed at the output plane. Each

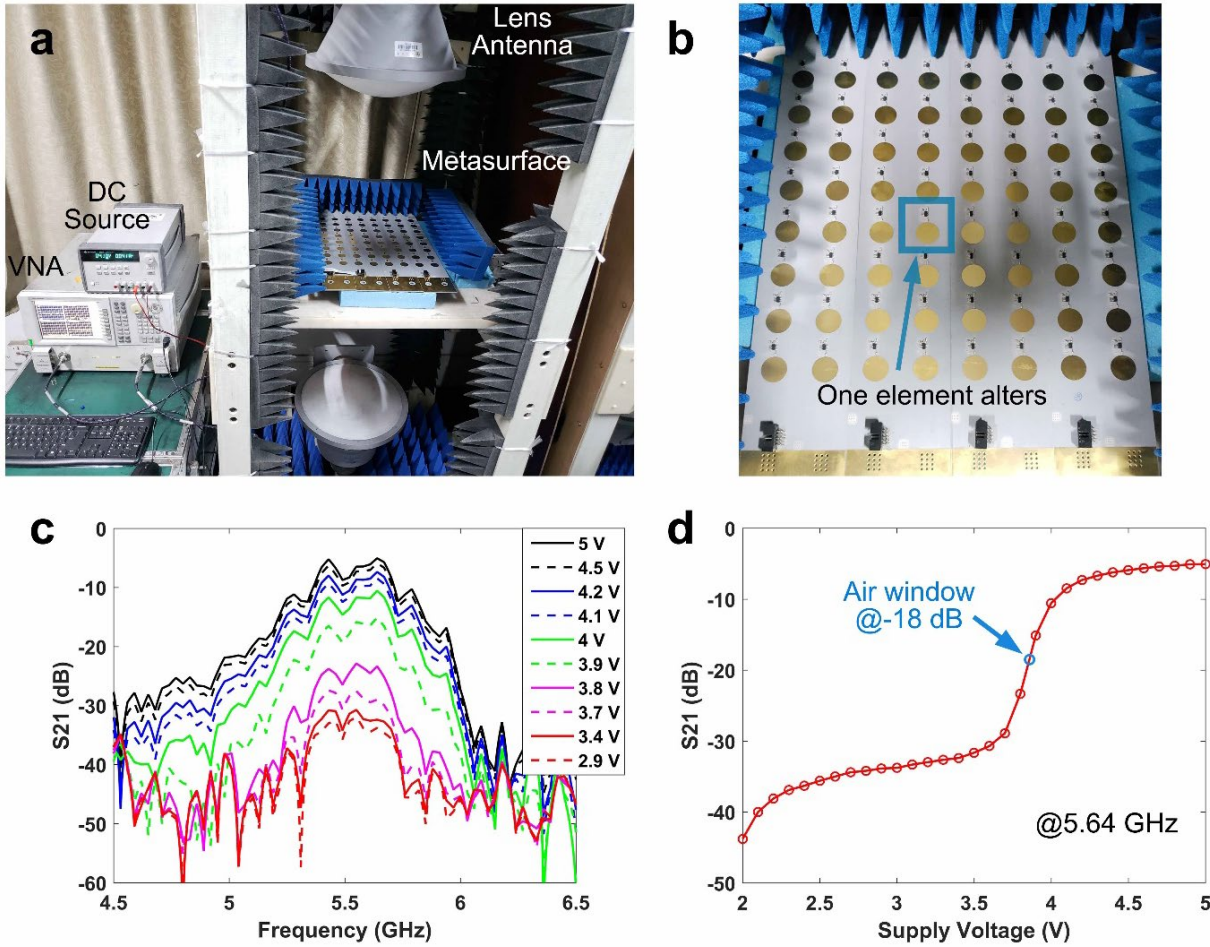
of them corresponds to one digit. **a**, The visualization of the amplitude transmission coefficients of all meta-atoms at the first layer using a handwritten digit '6' as example, in which the high pixel value represents the relatively high amplitude transmission coefficient. **b**, The EM energy distribution on the output plane when inputting the digit '6' in (**a**). The receiver representing the digit '6' has received the maximum energy, indicating that the input digit is successfully classified. **c,d**, Confusion matrix and energy distribution percentage for testing results using 10,000 different handwritten digit images. **e**, The results show that the detector region corresponding to the correct digit category will receive the maximum energy. This simulation proves that our PAIM has the capability to deal with complicated classification tasks even by only adjusting the amplitude of the transmitted wave. **f**, The change of valid loss and valid accuracy in the process of training, tested by 1000 randomly selected valid samples. The steady descent of valid loss proves the feasibility and stability of our PAIM structure applied in deep learning applications.



Supplementary Figure S4 | The simulation results for oil paintings recognition. Before inputting to our PAIM, the original images are grayed and normalized to [0, 1]. The results indicate that PAIM has the potential to handle high-level human intelligence like art appreciation.

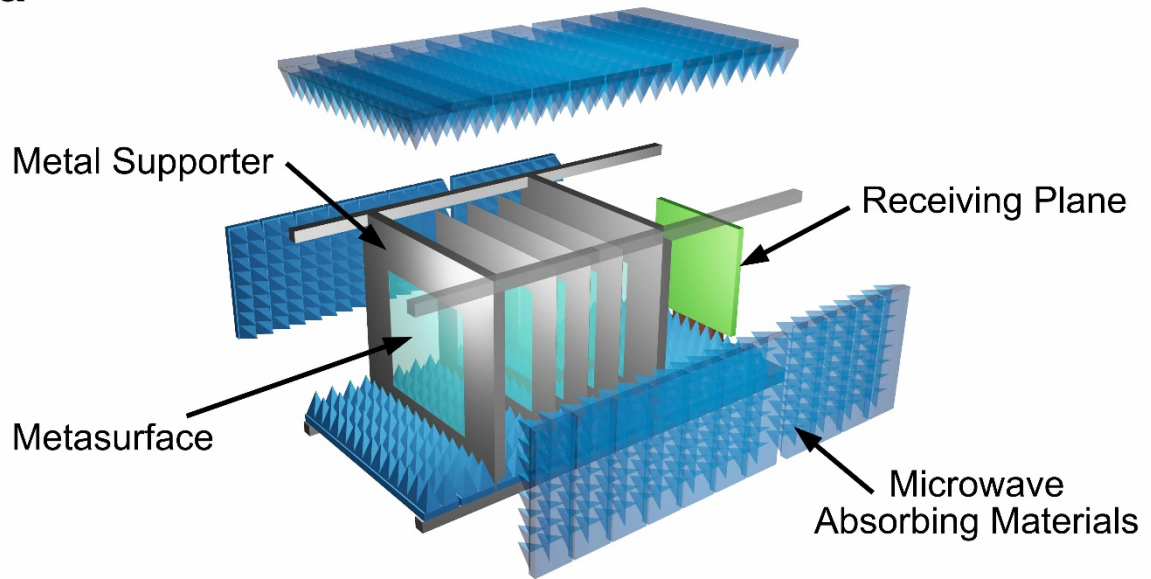


Supplementary Figure S5 | The detailed structure of meta-atom. a, The over view of the programmable node. **b,** The energy transmission and modulation on the meta-atom. **c,** The dimensions of the front view of the meta-atom. **d,** The circuit components for the amplifier.

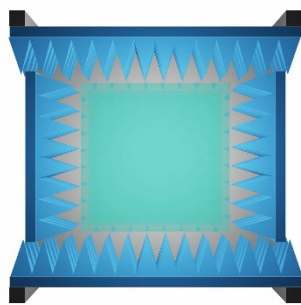


Supplementary Figure S6 | Modulation range measurement of meta-atom. **a**, Experiment configuration for the measurement, where a vector network analyzer and DC power source are employed. **b**, The detailed view of the measured metasurface, where only one element is activated and the others are powered off. **c**, The measured transmission coefficients (S_{21}) from 4.5 to 6.5 GHz based on the measurement system, when only one meta-atom is modulated. **d**, The transmission amplitude modulation range at 5.64 GHz when the implemented voltage alters from 2 to 5 V.

a

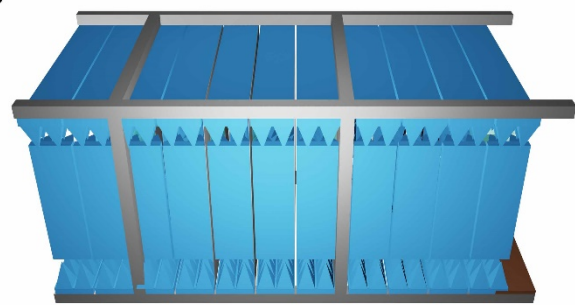


b



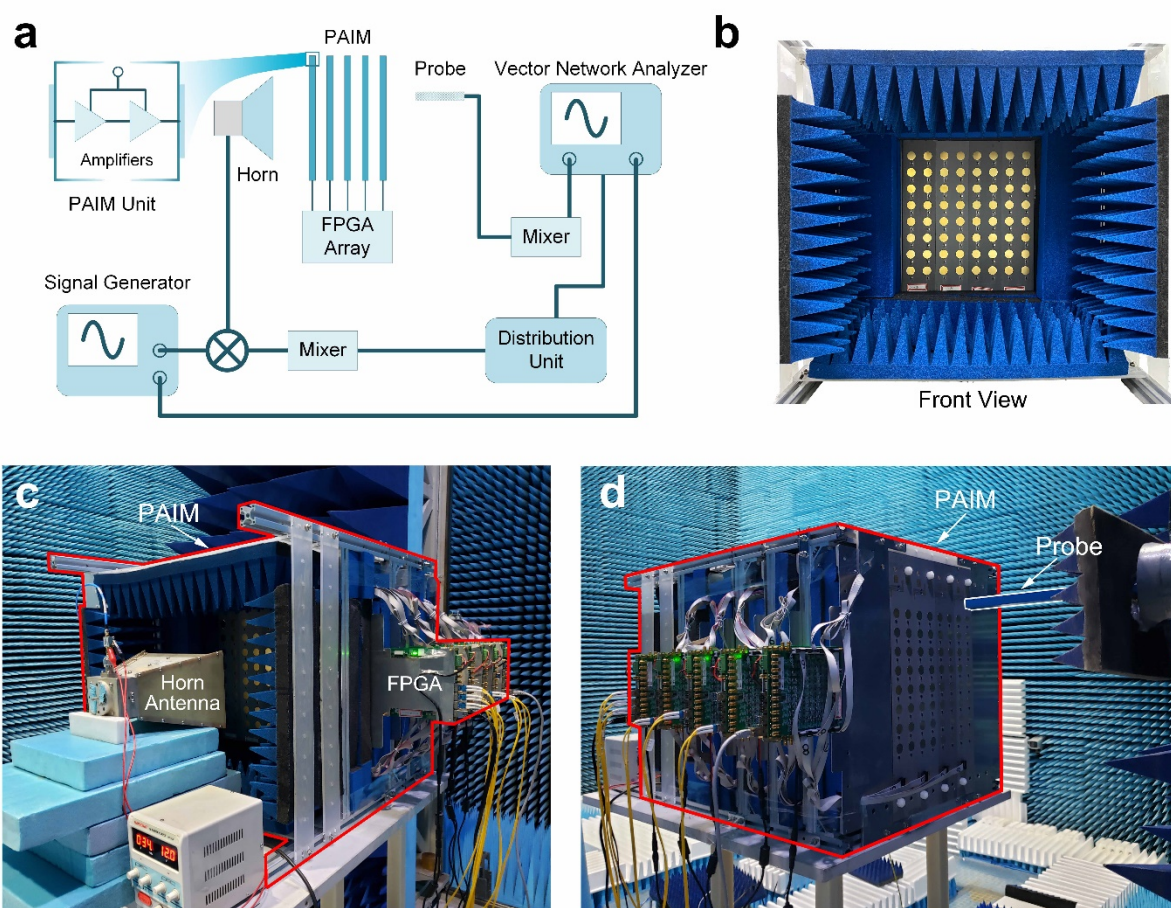
Front View

c



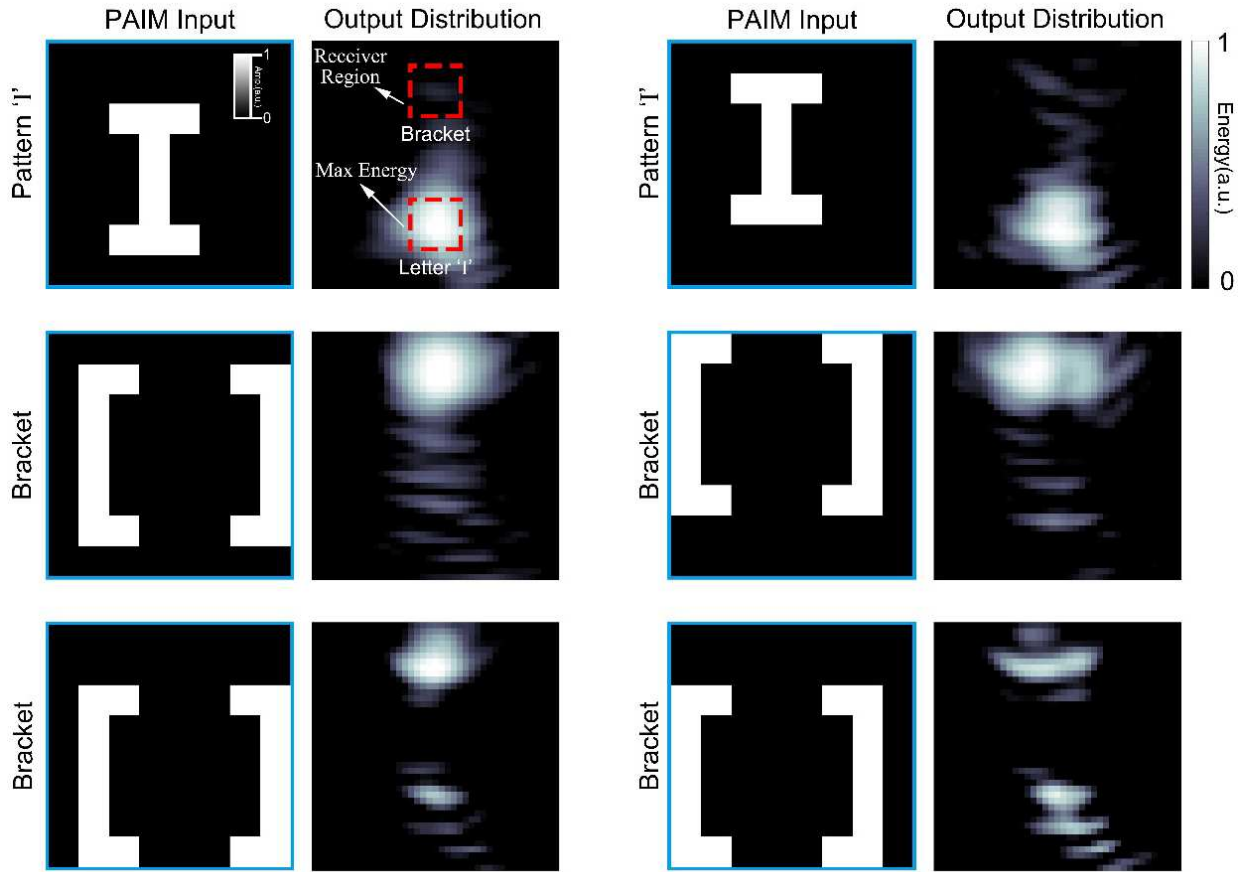
Side View

Supplementary Figure S7 | The illustration of PAIM support structure. a, The exploded view of the designed support structure for PAIM. **b,c,** The front and side views of the designed support structure.

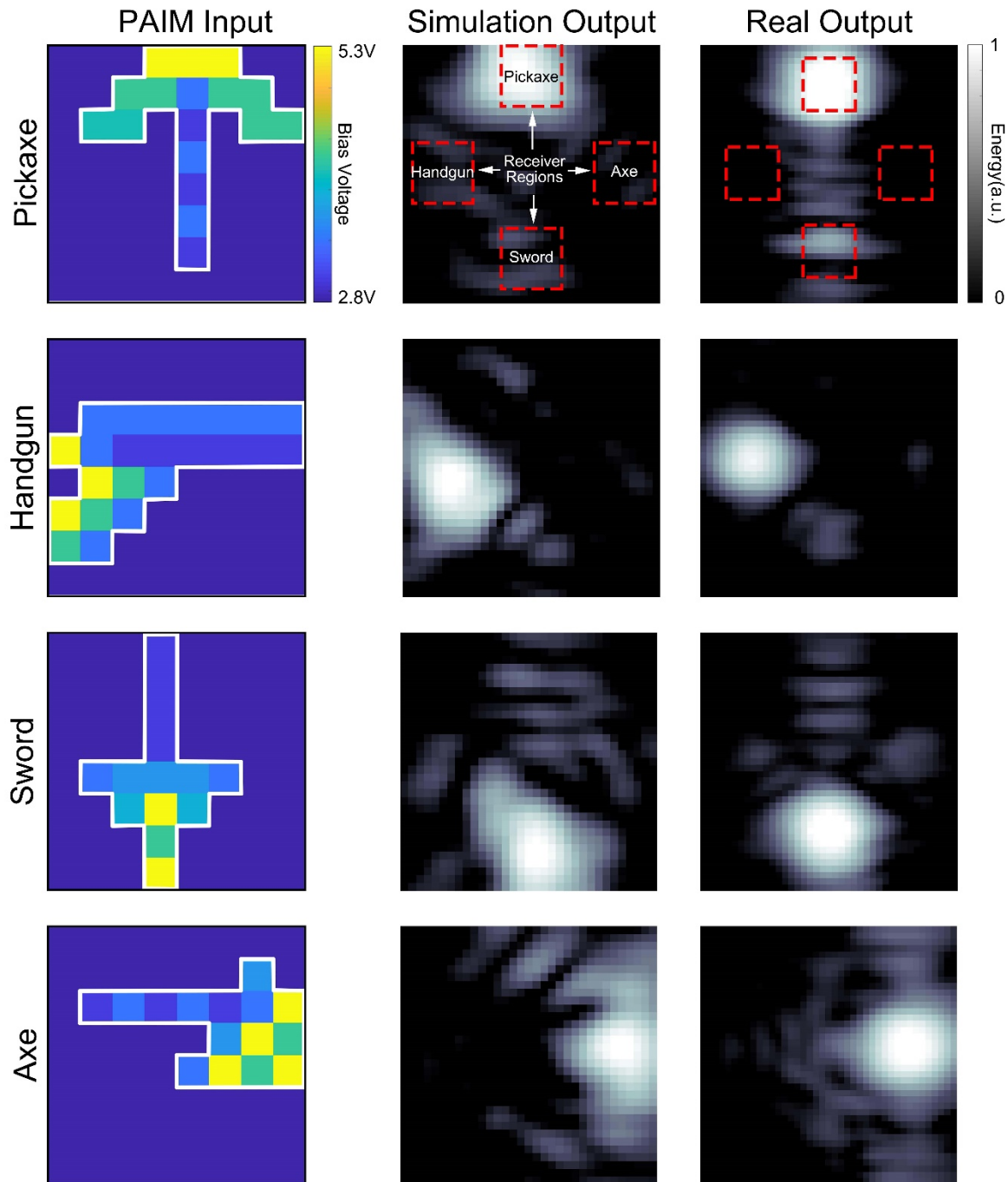


790

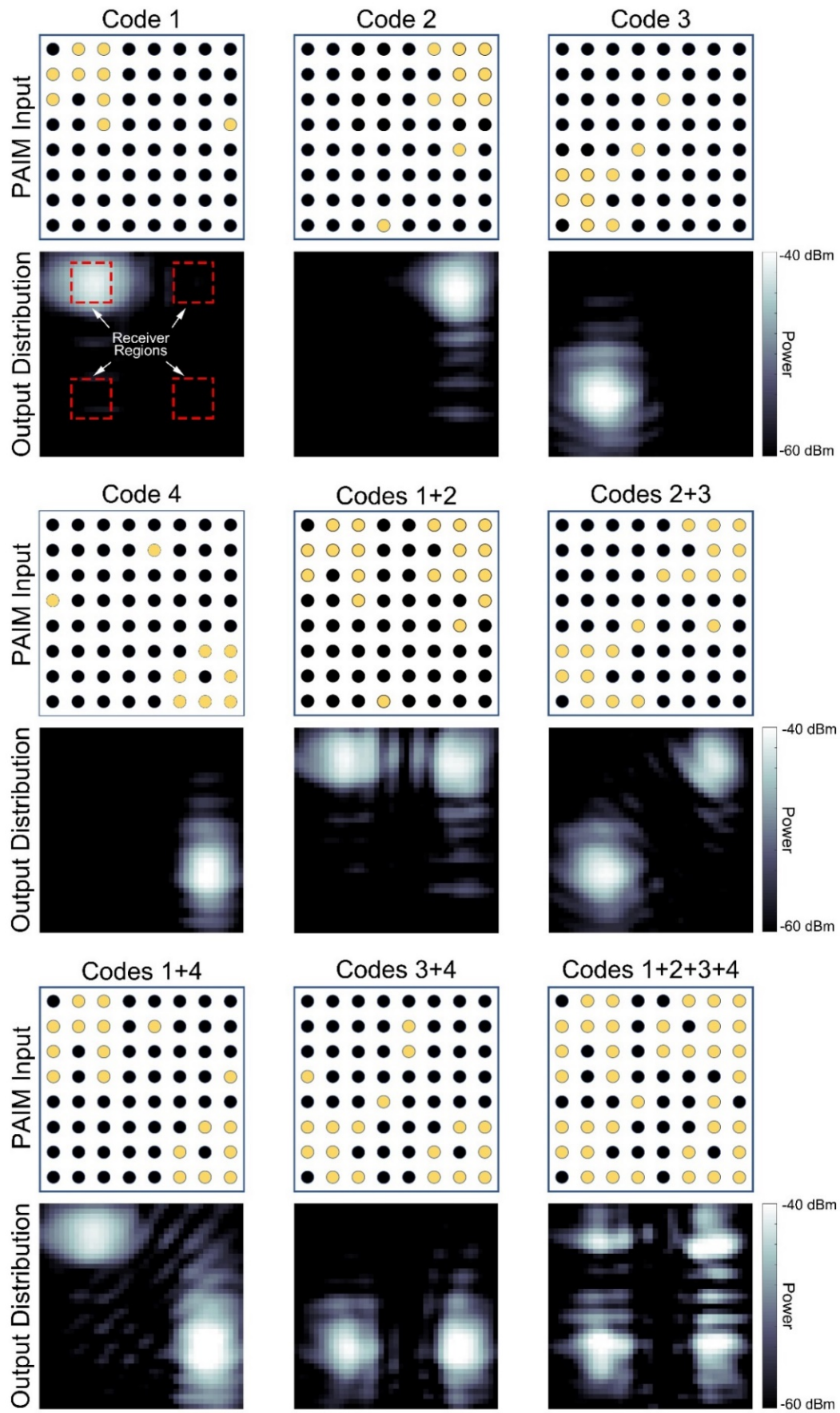
Supplementary Figure S8 | The manufactural entity and experimental environment of PAIM. **a,** The schematic of testing system. **b,** The front view of PAIM. **c,d,** The photographs of the experimental environment of PAIM. A horn antenna connected with a power-amplifier is used to generate the continuous-wave radiation at 5.4 GHz. The FPGA arrays could generate different levels of bias voltages applied to the meta-atoms, modulating the transmission coefficient of each meta-atom individually. The energy distribution on the output plane is measured by a moving electromagnetic stylus. A vector network analyzer is used to measure the amplitude and phase.



Supplementary Figure S9 | Experimental results of the simple pattern recognition task. The measured results prove that our PAIM could transfer the energy distributions from different patterns to their corresponding receiving antennas. However, the offset of pattern positions would hinder the focus of energy and increase the difficulty of recognition. The pattern of bracket '[']' located at the lower left of the input plane was just correctly recognized.



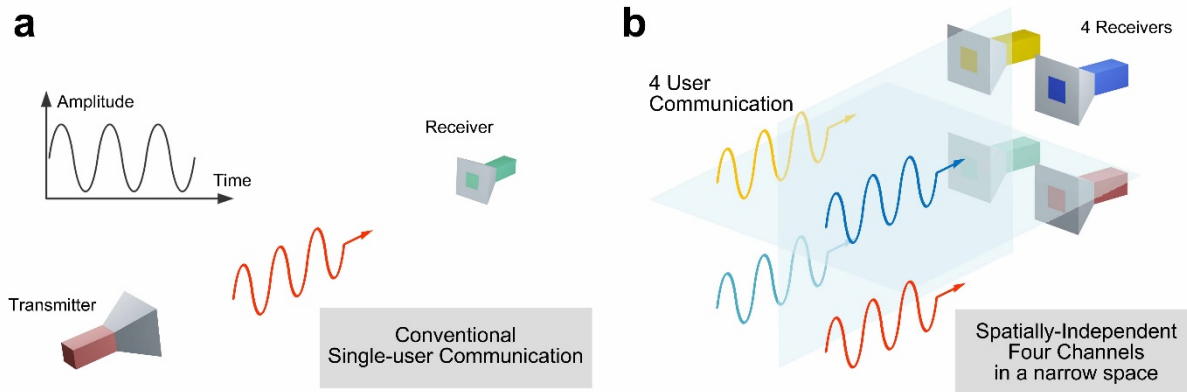
Supplementary Figure S10 | Comparison between simulated and measured output energy distributions in game props recognition. The regions of high energy have good match between the simulated and measured output energy distributions, proving the feasibility of the designed bias voltages by training on computer. The distribution differences in small energy regions are mainly caused by the bias voltage error, inconsistency of meta-atoms, pose change of transmitting horn antenna, and diffraction of waves from the edges of PAIM.



Supplementary Figure S11 | The experimental results for mobile communication code task. The

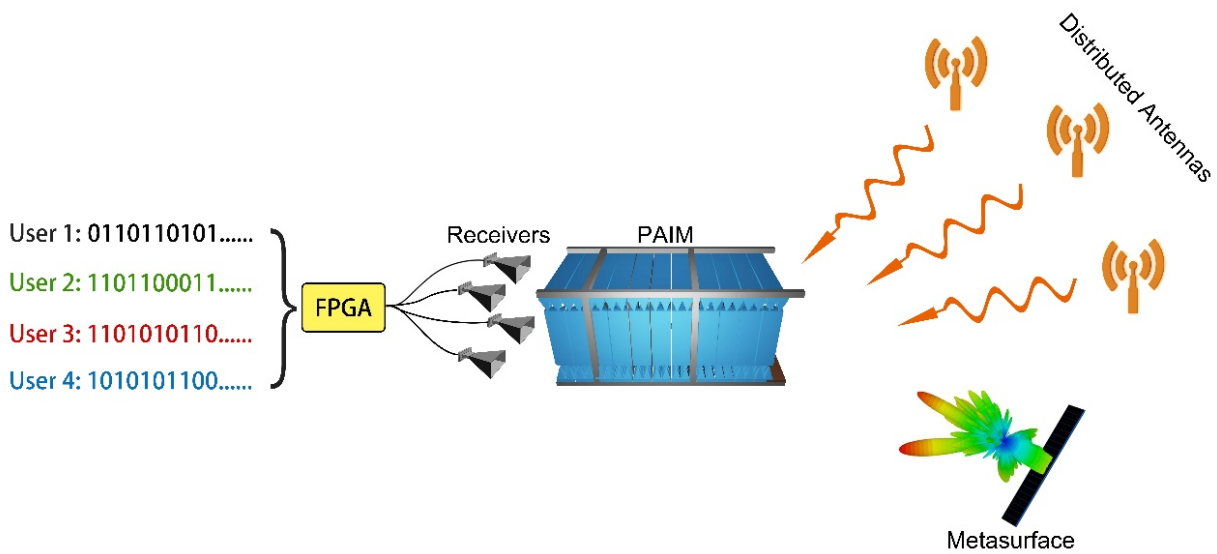
measured results for different combinations of user codes are presented in this figure. By setting an energy threshold for each receiving antenna, we could know whether the corresponding user code is transmitted. The speed of decoding is as fast as the light speed, giving the potential to reduce the time delay in wireless communications.

820



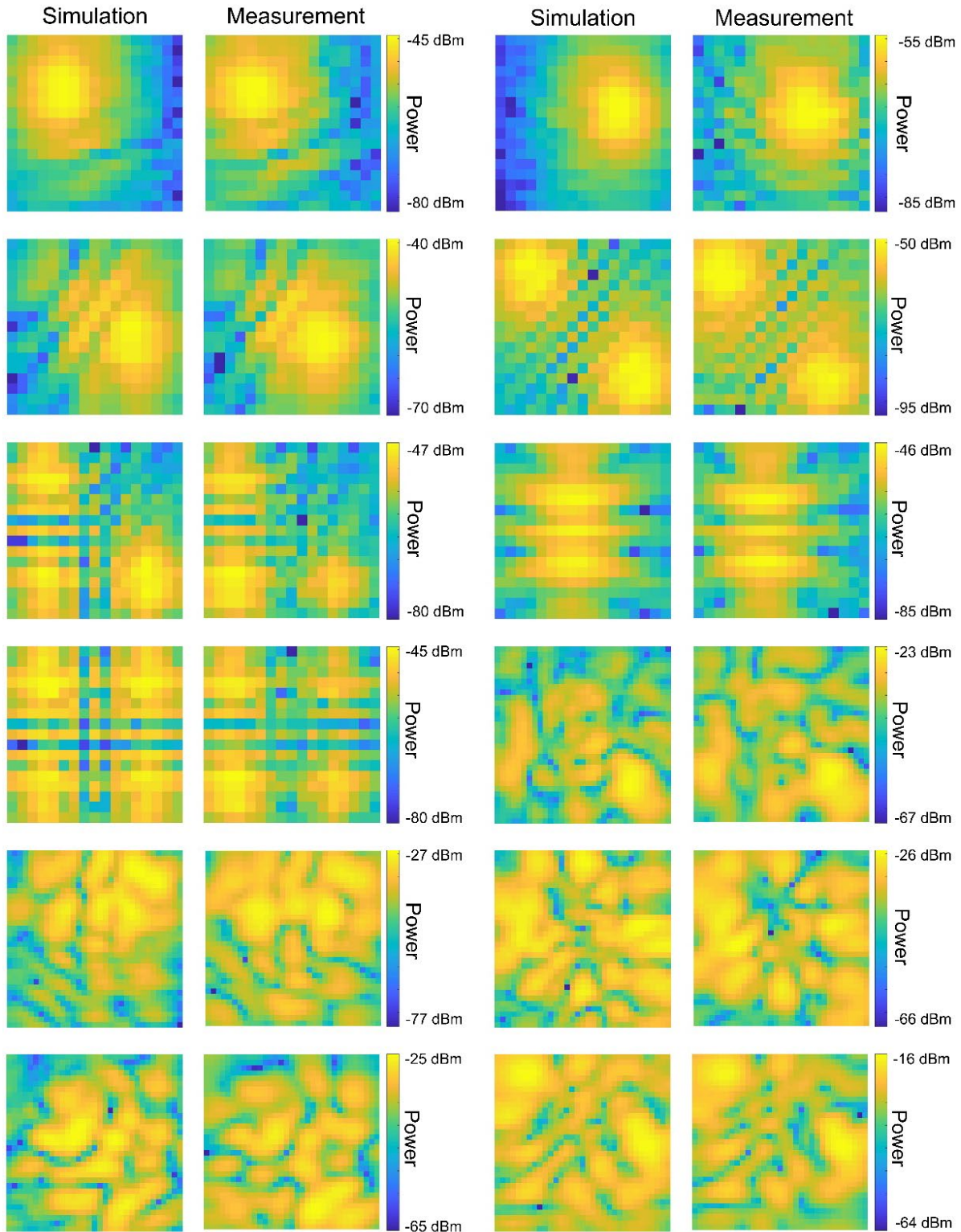
Supplementary Figure S12 | Comparison of communication codec tasks between the traditional and the presented methods. a, The traditional CDMA structure, in which the information is modulated at the dimension of time. Thus, the time consumption to send a message bit is proportional to the length of code. **b,** The proposed CDMA structure. Our PAIM could take the space-for-time strategy to spread the codes into space energy distribution. Thus, the time consumption of sending a message is very tiny and has a fixed value, which could reduce the time period for sending a message and increase the channel capacity.

830



Supplementary Figure S13 | The schematic of two strategies to increase the transmission distance.

The EM waves from different orientations radiated by the distributed antennas (or base stations) would be superposed and thus generate variegated EM energy distributions at the position of PAIM. The large reflected metasurfaces also possess the capacity of generating various complicated EM distributions, like the holographic imaging. Our PAIM could receive the EM field distributions, distinguish them to the related user coding combinations, and transfer the energies to the related receiving antennas. FPGA could process the signals from the receiving antennas and output the binary information of each user. The whole system indicates that our PAIM has the ability to fully use the space information of EM waves and give a new way to realize the space division multiplexing.



850

Supplementary Figure S14 | Comparison between the measured and simulated EM energy distributions. Although there are slight differences between the measured and simulated energy distributions, the regions of high energy are nearly at the same places. Because the applications of PAIM are mainly focused on the high energy regions of the output energy distributions, the accuracy of our simulations could meet the requirements in actual applications.

References for Supplementary Materials

- 39 Kingma, D. P. & Ba, J. Adam: A Method for Stochastic Optimization. Preprint at
<https://arxiv.org/abs/1412.6980v8> (2014)
- 40 Sprechmann, P., Bronstein, A. M. & Sapiro, G. Learning efficient sparse and low rank models.
860 *IEEE Transactions on Pattern Analysis and Machine Intelligence* **37**, 1821-1833 (2015).

Figures

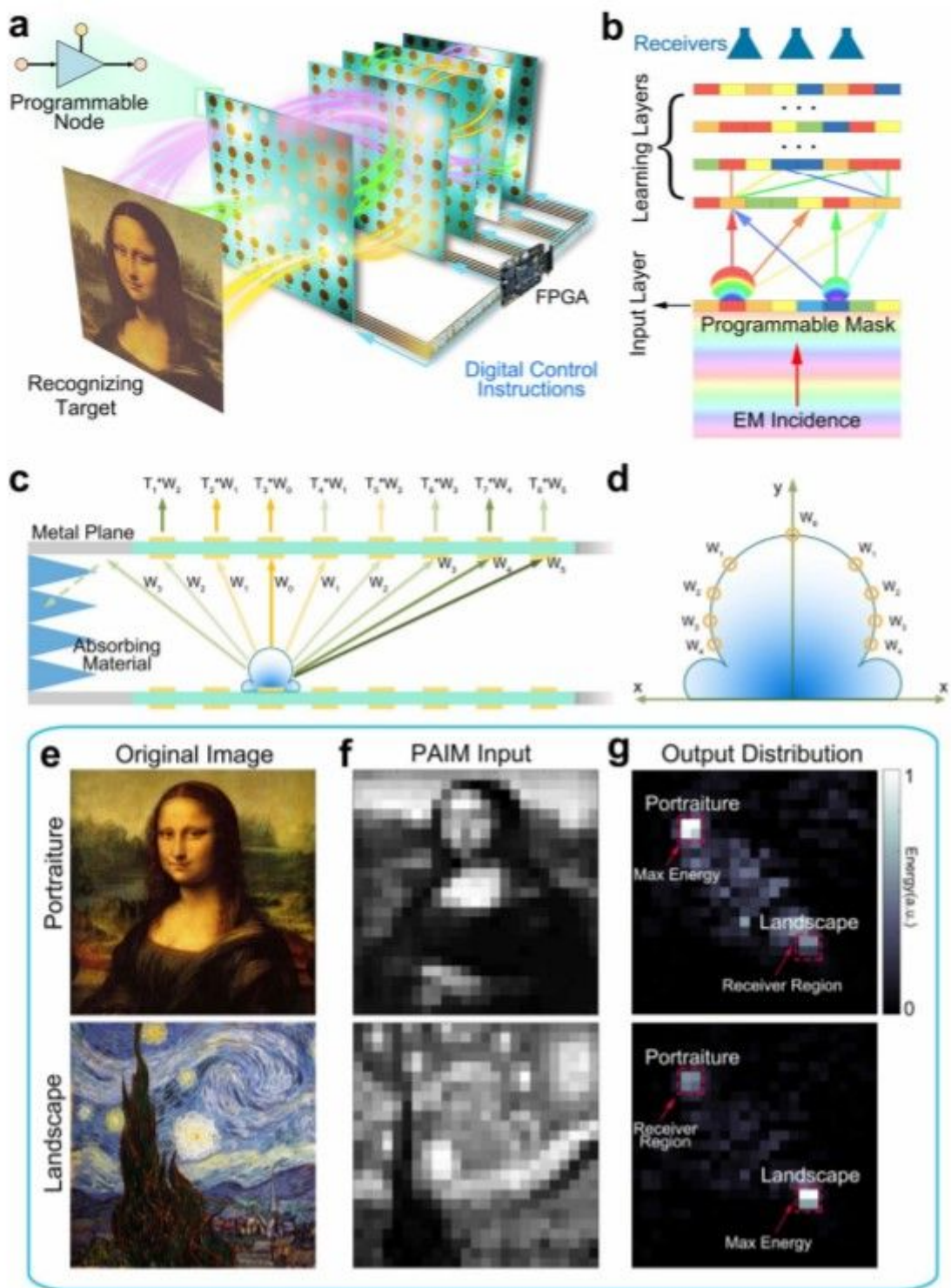


Figure 1

| PAIM – A reprogrammable D2NN platform. a, An array of programmable metasurfaces is used to construct PAIM, in which several FPGAs are installed to control the gain factor of each meta-atom, making PAIM a real-time and re-trainable intelligent machine. b, The schematic diagram 320 of PAIM. A

meta-atom in the learning layer will receive the waves radiated from all meta-atoms in the former layer, making the PAIM structure a full-connected network. The transmission coefficient of each meta-atom can be trained by using supervised/unsupervised learning or even reinforcement learning methods to achieve various functions. The first layer acts as the input layer by using pre-set transmission coefficients to encode the input information into the spatial distribution of EM energy. c, The transmitted wave of a meta-atom, multiplied by propagation factors, illuminates on all meta-atoms in the next layer. Then the EM wave is multiplied by the complex-valued transmission coefficient to act as the secondary source of wave. d, The radiation pattern of a meta-atom. e-g, Two testing examples for oil painting classification, in which (e) and (f) are the original pictures and their corresponding normalized visualization images of amplitude transmission coefficients in the 330 input layer, and (g) illustrates the energy distributions in the output plane, demonstrating that the two pictures are successfully classified.

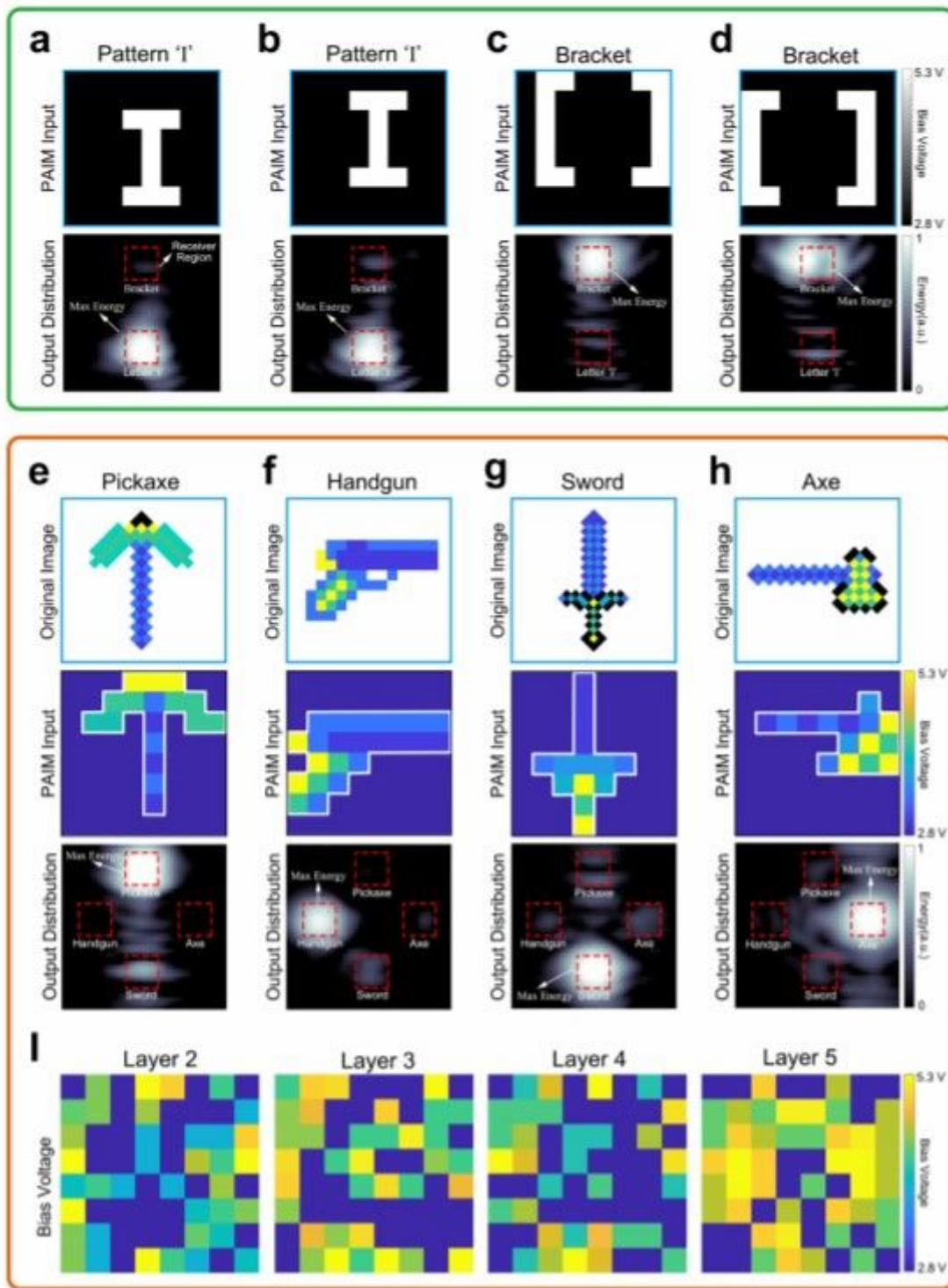


Figure 2

Experimental results of image classifications using PAIM. a-d, Two kinds of patterns (letter 'I' and bracket '[]') are represented by the distributions of bias voltages for 8×8 meta-atoms in first PAIM layer. The input image consists of 8×8 blocky squares of colors and each square represents the bias voltage of the meta-atom. The meta-atoms in the remaining four layers are assigned the bias voltages designed from the training process and could recognize the two patterns by ranking the receiving energies from the two

receiving antennas. The patterns of letter 'l' in (a) 340 and (b) and the patterns of 'I' in (c) and (d) have different locations. e-h, The original images of game prop are down-sampled to 8×8 blocky squares of colors, representing different levels of bias voltages for 8×8 meta-atoms in first PAIM layer. The pictures of output distributions indicate the expected testing results. i, The bias-voltage configurations of layers 2 to 5, which are obtained by the training process running on a computer.

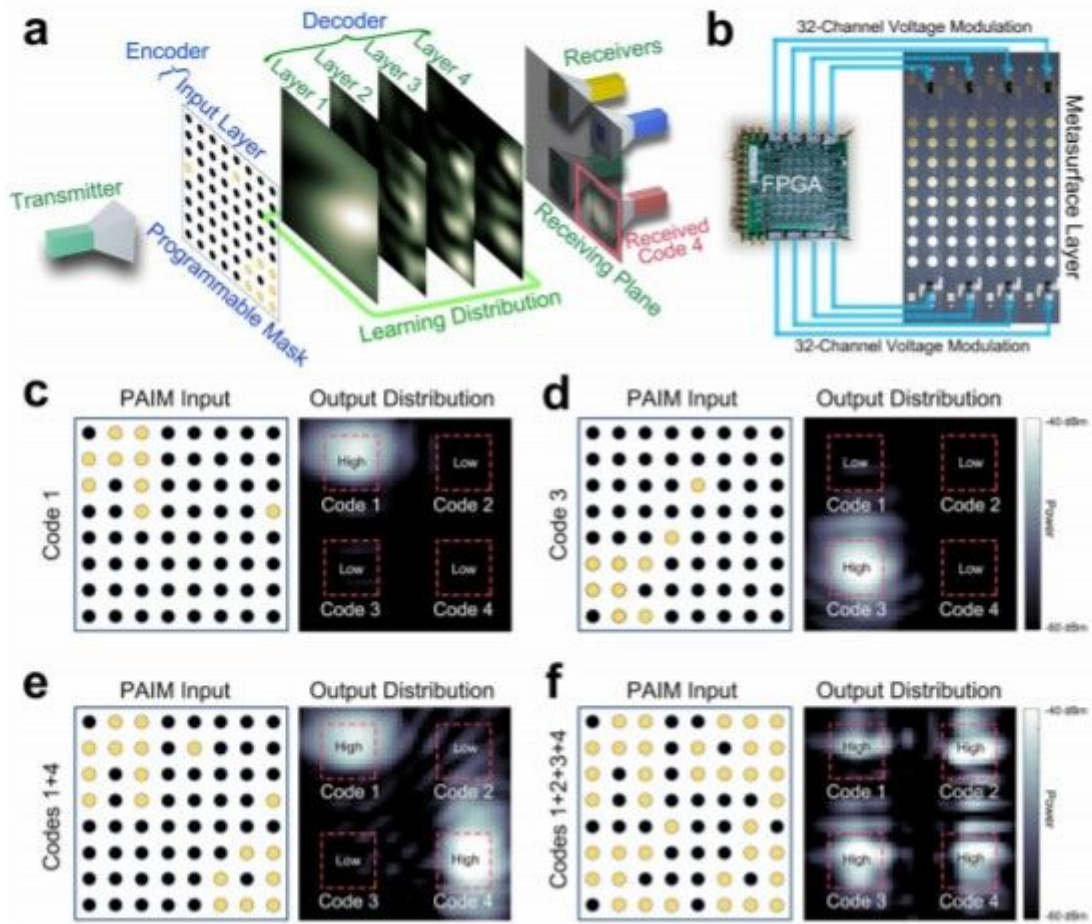


Figure 3

Experimental results of encoder and decoder in the CDMA task using PAIM. a, The energy distributions of all layers when radiating the coding information of the fourth user. The input layer acts as an encoder to transform the user code to the energy distribution in the free space. The yellow and black dots in the input layer represent the binary digits '1' and '0', respectively. PAIM receives the spatial energy distribution and decodes it by four metasurface layers to judge which user code has been transmitted. The input patterns of the four user codes are presented in Supplementary 370 Fig. S11. b, Photograph of one of the fabricated metasurface layers, which is controlled by altogether 64-channel voltages with the corresponding FPGA. c,d, The energy distributions of user codes 1 and 3 on the output plane when transmitting one user code, showing that only the correct receiver corresponding to the transmitted user code could collect high energy. e,f, The output energy distributions when simultaneously transmitting two

(1 and 4) or four (1, 2, 3, and 4) user codes. Only the receivers corresponding to the transmitted user codes collect high energies, indicating that all user codes could be decoded correctly and simultaneously.

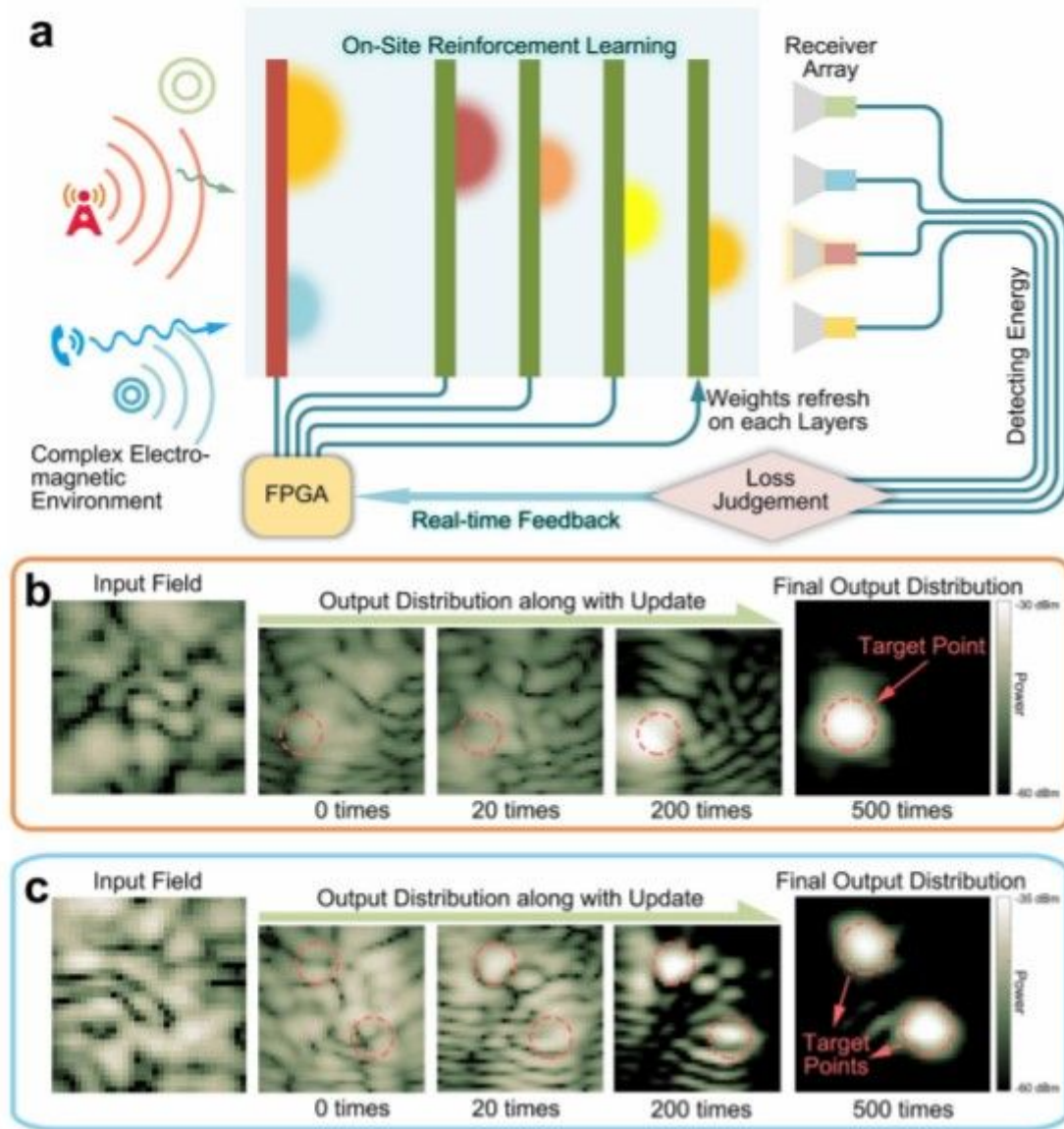


Figure 4

Experimental results of dynamic multi-beam focusing by the on-site reinforce-learning process using PAIM. a, The on-site reinforce-learning process of PAIM, in which the transmission 380 coefficients of each PAIM layer are continually controlled by FPGA according to the real-time feedback signals. b, c, The evolution of the output energy distributions along with the updated time in the reinforce-learning process. Here, the distributions of input fields in (b) and (c) are randomly generated but remained unchanged during the reinforce-learning process. We observe that the energies of the output fields are gradually focused on the target points when the updating procedure goes on.